Designing An η–Cu$_6$Sn$_5$ Alloy Anode for Sodium Ion Batteries

ENMA490 Team Dramastic – Spring 2013

Nicholas Weadock – Team Leader

Rajinder Bajwa – Prototyping & Characterization

Caleb Barrett – Design & Characterization, Secretary

David Lockman – Prototyping & Data Analysis

Joseph White – Modeling Team, Videographer, Treasurer

Matthew Zager – Modeling Team Lead

Table of Contents

I. Abstract:

Sodium ion batteries are a promising technology for grid scale storage; however, they are plagued by short lifetimes due to anode pulverization. We have investigated the feasibility of the η-Cu_6Sn_5 alloy as a high capacity, high cycle life anode for sodium ion batteries. This system has been shown to improve the cycle life for lithium ion batteries as compared to pure Sn anodes. First principles calculations demonstrate that at least 6 Na atoms can fit within the η-Cu_6Sn_5 structure. Additionally, the volume expansion for a 2 Na atom structure is less than the corresponding expansion in Sn anodes. Intermetallic compound growth models indicate that this alloy can be fabricated using scalable electrodeposition and annealing processes, if the Cu/Sn ratio is optimized.

II. Motivation and Previous Research:

The development of a renewable energy based power infrastructure has been proposed as a way to slow the production of CO_2.[1] This type of infrastructure requires the storage of excess energy produced at times of high winds or solar irradiance.[1] Sodium ion batteries (NIBs) provide a viable alternative to current storage technologies, due to the low cost and abundance of sodium.[2] These batteries can meet the price goal of \$100/kWh set by researchers in the field.[3]

Research to date has focused on two types of anodes for NIBs; carbon-based intercalation anodes and metal-based alloying anodes.[4, 5] Carbon based anodes do not experience as large a volume expansion as metal ones; however the theoretical capacity is much lower.[5] Tin has been explored as a potential anode, with a theoretical capacity of 846.77 mAh/g. This capacity corresponds to the formation of the $Na_{15}Sn_4$ phase.[2, 5] The theoretical capacity of Sn anodes for NIBs has not been reached; losses occur as a result of slow diffusion and reaction kinetics, the formation of the solid electrolyte interphase (SEI), and most importantly the decrepitation of the anode due to a volume expansion of over 400%.[5] Chevrier reported that due to the extreme volume changes associated with cycling, electrochemically active metal anodes are not a viable option for NIBs and novel alternatives must be explored.[2]

Previous research has shown that adding Cu to Sn increases the cycling capacity of Sn based anodes in lithium ion batteries.[6, 7] The Cu does not alloy with lithium or sodium, and serves as an expandable matrix for the Li-Sn phases.[7] Three phases exist for the CuSn alloys at room temperature: Cu_4Sn, Cu_3Sn, and Cu_6Sn_5.[8] Increasing the Cu concentration increases cyclability, but decreases the energy density of the battery.[7] As such, the Cu_6Sn_5 alloy is the most widely studied for lithium ion batteries. Recently, a group at Oak Ridge National Laboratory investigated the high temperature hexagonal η'-Cu_6Sn_5 phase as an anode for NIBs.[9] The voltage profile associated with sodiation of the alloy matches well with that of the Na-Sn system.[9] Mossbauer spectroscopy and X-Ray diffraction results indicate that the $Na_{15}Sn_4$ phase forms within a copper matrix without the appearance of a ternary phase. Additionally, Na diffusion pathways into the high and low temperature η'/η-Cu_6Sn_5 phases were proposed.[9]

III. Materials Science Aspects:

The goal of this project is to design and prototype a low temperature monoclinic η-Cu_6Sn_5 alloy anode for use in NIBs that will have a high capacity and cyclability. The formation of Na-Sn alloys within a Cu matrix will reduce the volume changes and mechanical stresses compared to

an entirely Sn anode.[7] At the onset of the project, no investigations of this system had been reported, and no thermodynamic phase diagrams existed for the Na-Cu or Na-Cu-Sn systems. Only two ternary phases had been reported, the $Na_{12}Cu_{12}Sn_{21}$ Zintl FCC phase and the $Na_{2.8}Cu_5Sn_{5.6}$ nanotube phase.[10, 11] These phases are synthesized at high temperatures and the Zintl phase is a semiconductor with a bandgap of 1.34eV; as such they are not desirable for a low cost anode.[10, 11]

First principles calculations will first allow us to determine if Na can be favorably inserted into the Cu_6Sn_5 structure; subsequent calculations will determine the potential insertion sites and voltages for Na atoms into the Cu_6Sn_5 structure and the energy pathways associated with sodiation. Prototype anodes will be produced by electrodepositing Sn onto Cu foil and annealing for a time calculated determined by kinetic diffusion modeling. The identity and thickness of each phase will be investigated with XRD and SEM, respectively.   These techniques are commonly used in materials design and fabrication research, and the development of suitable anodes for sodium-ion batteries is a materials engineering project.

IV. Technical Approach – Modeling and Design:

First Principles Simulations Summary:

The main design goal is to use density functional theory (DFT) to perform first principles calculations that determine the total energy of the sodiated and desodiated Cu_6Sn_5 phase. From the different energies we can determine average voltage of sodiation/desodiation in the low temperature monoclinic Cu_6Sn_5 phase. Also, we will relax the different sodiated structures to determine the volume expansion of the cell. The crystal structure and the alloy composition are the only necessary inputs to complete first principle calculations.[12]   To complete the first principle calculations we will use the Vienna Ab-initio Simulation Package (VASP).

Using the INCAR, POSCAR, POTCAR, and KPOINTS input files we will relax each unit cell to determine the parameters that yield the minimum energy. Then, we will build the unit cell with the optimized parameters and run a bulk energy calculation. The bulk energy is what we will use in the voltage calculation. After we determine the bulk energy we will allow the volume of the sodiated structures to expand and calculate the lattice parameter and c/a ratio that produce the most negative energy.   From this value, we can evaluate the expected volume expansion associated with the Na insertion and compare it to the typical expansion in a Sn-only anode.

VASP Input Summary:

Materialsproject.org provides us with the required inputs including the unit cell, atom location, and lattice parameters Cn_6Sn_5 (unit cell: $Cu_{12}Sn_{10}$).[13-15] The Crystal Toolkit from Materials Project allows us to generate all VASP input files (INCAR, KPOINTS, and POSCAR) except for the POTCAR file.[14] The POTCAR file provides the pseudopotentials for the alloy and it is not available for free through Materialsproject due to copyright issues.[13] However, we obtained the POTCAR   files   for   Cu,   Sn,   and   Na   courtesy   of   Professor   Einstein's   group.

The VASP files downloaded from Materials Project provided us with a good initial direction. The POSCAR file provided by Materials Project for $Cu_{12}Sn_{10}$ and Na were used without any

changes. The POSCAR file provides the lattice vectors and the fractional coordinates that specify the position of each individual atom.[12]

The suggested grid density from the KPOINTS file provided by Materials Project was also used without any changes. However, the INCAR file had to be altered based on the type of calculation we were performing. The INCAR file is the main input file for VASP and it communicates what calculations to do and how to do them.[12] The different INCAR files can be seen below in Table 1, Table 2, and Table 3:

Table 1: The INCAR files used during the relaxation of a Na atom (left) and the bulk energy calculation (right) that determined the ground state energy of a Na atom.

Relaxation for Na atom	Bulk Energy for Na atom

ISTART = 1   # start job from past configuration
PREC   = High   # precision high
ENCUT = 400   # cutoff used in all calculations
LREAL = .FALSE.   # real space projection yes
NELMIN = 4   # minimum electronic steps
EDIFF = 1e-4   # allowed error in total energy
NPAR   = 4
### RELAXATION 	
ISMEAR = 0   # single molecule
SIGMA = 0.20   # small sigma
EDIFFG = -1e-2   # max allowed force
NSW   = 100   # 100 ionic steps in ions
IBRION = 2   # Relaxation method
ISIF   = 2   # relax ions, but no cell shape or size
POTIM = 0.2   # Step size
### OTHER PARAMETERS 	
ISPIN = 1   # spin polarized
	ISTART = 1 # start job from past configuration
	PREC = High # precision high
	ENCUT = 400 # cutoff used in all calculations
	LREAL = .FALSE. # real space projection yes
	NELMIN = 4 # minimum electronic steps
	EDIFF = 1e-4 # allowed error in total energy
	NPAR = 4
	### RELAXATION
	ISMEAR = -5 # single molecule, bulk energy
	SIGMA = 0.20 # small sigma
	EDIFFG = -1e-2 # max allowed force
	NSW = 100 # 100 ionic steps in ions
	IBRION = 1 # Relaxation method
	POTIM = 0.2 # Step size
	### OTHER PARAMETERS
	ISPIN = 1 # non-spin polarized

Table 2: The INCAR files used during the relaxation of a $Cu_{12}Sn_{10}$ (left) and the bulk energy calculation (right) that determined the ground state energy of a $Cu_{12}Sn_{10}$.

Relaxation of $Cu_{12}Sn_{10}$	Bulk Energy for $Cu_{12}Sn_{10}$

ISTART = 1   # start job from past configuration
PREC   = High   # precision high
ENCUT = 400   # cutoff used in all calculations
LREAL = .FALSE.   # real space projection yes
NELMIN = 4   # minimum electronic steps
EDIFF = 1e-4   # allowed error in total energy
NPAR   = 4
### RELAXATION 	
ISMEAR = 1   # 22 atom system
SIGMA = 0.20   # small sigma
EDIFFG = -1e-2   # max allowed force
NSW   = 100   # 100 ionic steps in ions
IBRION = 2   # Relaxation method
ISIF   = 2   # relax ions, fixed volume
POTIM = 0.2   # Step size
### OTHER PARAMETERS 	
ISPIN = 1   # non-spin polarized
	ISTART = 1 # start job from past configuration
	PREC = High # precision high
	ENCUT = 400 # cutoff used in all calculations
	LREAL = .FALSE. # real space projection yes
	NELMIN = 4 # minimum electronic steps
	EDIFF = 1e-4 # allowed error in total energy
	NPAR = 4
	### RELAXATION
	ISMEAR = -5 # 22 atom system, bulk energy
	SIGMA = 0.20 # small sigma
	EDIFFG = -1e-2 # max allowed force
	NSW = 100 # 100 ionic steps in ions
	IBRION = 1 # Relaxation method
	POTIM = 0.2 # Step size
	### OTHER PARAMETERS
	ISPIN = 1 # non-spin polarized

Table 3: The INCAR files used during the relaxation of 2 Na atoms in $Cu_{12}Sn_{10}$ (left) and the bulk energy calculation (right) that determined the ground state energy of 2 Na atoms $Cu_{12}Sn_{10}$.

Relaxation of 2 Na Insertions		Bulk Energy of 2 Na Insertions	
ISTART = 1	# start job from past configuration	ISTART = 1	# start job from past configuration
PREC = High	# precision high	PREC = High	# precision high
ENCUT = 400	# cutoff used in all calculations	ENCUT = 400	# cutoff used in all calculations
LREAL = .FALSE.	# real space projection yes	LREAL = .FALSE.	# real space projection yes
NELMIN = 4	# minimum electronic steps	NELMIN = 4	# minimum electronic steps
EDIFF = 1e-4	# allowed error in total energy	EDIFF = 1e-4	# allowed error in total energy
NPAR = 4		NPAR = 4	
### RELAXATION		### RELAXATION	
ISMEAR = 1	# 24 atom system	ISMEAR = -5	# 24 atom system, bulk energy
SIGMA = 0.20	# small sigma	SIGMA = 0.20	# small sigma
EDIFFG = -1e-2	# max allowed force	EDIFFG = -1e-2	# max allowed force
NSW = 100	# 100 ionic steps in ions	NSW = 100	# 100 ionic steps in ions
IBRION = 2	# Relaxation method	IBRION = 1	# Relaxation method
ISIF = 2	# relax ions, fixed volume	POTIM = 0.2	# Step size
POTIM = 0.2	# Step size	### OTHER PARAMETERS	
### OTHER PARAMETERS		ISPIN = 1	# non-spin polarized
ISPIN = 1	# non-spin polarized		

The INCAR file for the Na_6-$Cu_{12}Sn_{10}$ relaxation is not included in a table because it is the same as the file for the Na_2-$Cu_{12}Sn_{10}$ system. The INCAR files for the relaxation of Na, $Cu_{12}Sn_{10}$, Na_2-$Cu_{12}Sn_{10}$, and Na_6-$Cu_{12}Sn_{10}$ contain an ISIF=2 and IBRION=2 input. The ISMEAR=0 for a single atom system and ISMEAR=1 for the multiple atom systems. For the bulk energy calculations there is no ISIF input, IBRION=1 and the ISMEAR=-5 for both the Na and the multiple atom systems.

IBRION determines how the ions are updated and moved.[16] IBRION=2 for the relaxations because we are looking for the local minimum and the initial guess for the atomic positions are not necessarily close to the local minimum. IBRION=2 is suggested for difficult relaxations because it uses the "conjugate gradient algorithm that has the reliable backup routines."[14] IBRION=1 is used for the bulk energy calculations because the approximation for the fractional coordinates of the atoms are very close to the local minimum due to the relaxation.[16]

The ISMEAR controls the partial occupancies and how they are set for each orbital.[16] ISMEAR=-5 performs the tetrahedron method with Bloch corrections and it yields very accurate bulk energy calculations but it does not consider relaxations in metals.[16] Since ISMEAR=-5 does not consider relaxations in metals, we relaxed the structure first and then used ISMEAR=-5 to get the total bulk energy.[16]

When performing the relaxations we included the ISIF input because ISIF determines the degrees of freedom that are allowed to change (ions, cell volume, and cell shape). ISIF=2 for the relaxations because the only degree of freedom allowed to change is the ions, due to the fact we are manually changing the lattice constant and c/a ratio in the POSCAR file.

All the total energy calculations have been executed using the pseudopotential plane wave method, within the generalized gradient approximation (GGA).[17] The GGA is an estimation of

the exchange and correlation potential as the exact form is unknown.[12] The GGA considers gradients in the electron density when approximating the exchange and correlation potential. Thus, it attempts to correct the difference between the actual exchange and correlation potential and the potential determined using a uniform electron gas.[12]

Voltage and Voltage Profile Discussion:

There are three values we need to calculate using VASP in order to determine the voltage of sodiation/desodiation. The values are the total energy of a Na atom, the ground state energy of the Cu_6Sn_5 unit cell ($Cu_{12}Sn_{10}$), and the energy of the sodiated $Cu_{12}Sn_{10}$ structure. To calculate the energy of the sodiated $Cu_{12}Sn_{10}$ structure we will insert Na atoms into various locations of the host lattice, relax the sodiated structure, and perform bulk energy calculations.[18] From the different total energies we calculate the average voltage associated with the insertion of Na ions via the following equation (adapted from Zhu, et al.):[19]

$$\overline{V}_{Theory} = -\left(\frac{E_{defect} + xE_{Na} - E_{perfect}}{x} \right) \qquad (1)$$

E_{defect} is the energy of the structure after sodiation in eV, $E_{perfect}$ is the energy of the desodiated structure in eV/atom, E_{Na} is the energy of a single Na atom in eV, and x is the number of Na atoms per unit cell.

The above equation calculates the average voltage of sodiation of x Na atoms. This is a two point calculation that determines the voltage from the two limits of Na insertion; the energy of the fully sodiated and fully desodiated structure.[20] Complete sodiation here refers to all x Na atoms inserted into the unit cell. To calculate the sodiation voltage profile of this concentration completely, disorder of the atoms has to be considered. A cluster expansion that is parameterized by the total energy of 10-20 configurations of the disordered atoms would need to be performed to completely model the disorder.[20] The uncertainty of the insertion sites and the structures that will form indicate that cluster expansion is not feasible for this investigation.

A positive sodiation voltage indicates that a Cu-Sn alloy will be a successful anode material and the Na ion will insert into the host lattice. Simple thermodynamics confirms this fact, and the voltage can be expressed as a function of Gibbs free energy (ΔG):

$$V = \frac{-\Delta G}{(x_2 - x_1)F} \qquad (2)$$

Where V is the average voltage, F is Faraday's constant and (x_2-x_1) is the difference in Na concentration between two sodiated states or a sodiated and desodiated state.[20] If ΔG is negative, then the process is energetically favorable and the voltage will be positive. For a sodiation voltage less than or equal to 0.0V, ΔG is positive and we predict that sodium will not insert into the host lattice and instead plate on the alloy surface.[20]

The data we expect to get from the calculations are the energies of the structure at different concentrations of Na. The concentrations will correspond to the number of Na atoms per unit cell. Voltages calculated from Eq. (1) will be used to prepare a theoretical charge/discharge battery profile. The calculated voltage profile can be compared to experimental electrochemical data to evaluate the accuracy of the model.[17] Any discrepancies in the experiment may be due to

the formation of Na-Sn intermetallics. These alloys include $NaSn_5$, $NaSn$, Na_9Sn_4 and $Na_{15}Sn_4$.[2] The most likely interstitial sites to be occupied by Na atoms are not known, but can potentially be observed in the CONTCAR output file when the relaxed, lowest energy sodiated alloy structure is determined. A similar study has been done for both the Li-Sn and $Li-Cu_6Sn_5$ systems.[6, 17] In the Li-Sn system, it was found that the experimental voltage profile matched very well with computational predictions at low Li concentrations, but at high concentrations the loss of the long range order for Sn tetrahedra shifted the experimental profile. From this previous research we expect that the low Na content region will match well with the computational results, but the voltage drop associated with high Na concentrations may not be accurately predicted by DFT calculations.

Determination of Cu-Sn Intermediate Phase Growth:

It is important for us to analyze the growth kinetics of the Cu-Sn intermetallic compound (IMC) layers in order to design a proper anneal treatment. We can then anneal the samples at a given temperature for a specific length of time to yield the desired phases. This analysis will also allow us to estimate the phase layer thickness in the treated anodes.

Our target anneal temperature is 200 ºC. At this temperature, the Cu_6Sn_5 and Cu_3Sn IMCs form from Cu-Sn couples, according to the Cu-Sn phase diagram, without reaching the melting point of Sn.[mishigami phase diagrams] Several studies have previously been conducted analyzing the formation of Cu_6Sn_5 and Cu_3Sn layers at 200 ºC.[21-23]

We expect, initially, for Cu to diffuse much faster into Sn than Sn into Cu.[24] This difference likely arises from Cu diffusing into Sn by an interstitial mechanism, whereas Sn diffuses into Cu by a slower, substitutional method.[25] There is a negative change in free energy for Cu_6Sn_5 at 200 ºC (Paul) so nucleation is thermodynamically favorable. A Cu_3Sn phase will nucleate and grow between the Cu and Cu_6Sn_5 layers.[21-23] It is not clear in the literature whether or not the Cu_3Sn IMC would begin forming at the same time as the Cu_6Sn_5 layer.[23] Figure 1 shows the theoretical molar free energy profile for a Cu-Sn system as a function of at.% Sn at 200 ºC.[23] It can be seen that there is a larger driving force to nucleate Cu_6Sn_5, the η phase, than Cu_3Sn, the ε phase. Thus, it is possible that Cu_6Sn_5 nucleates first between Cu and Sn and that the Cu_3Sn forms later.[23] This agrees with the consistent observations of Cu_3Sn having a lower growth rate constant than Cu_6Sn_5.[21-23]
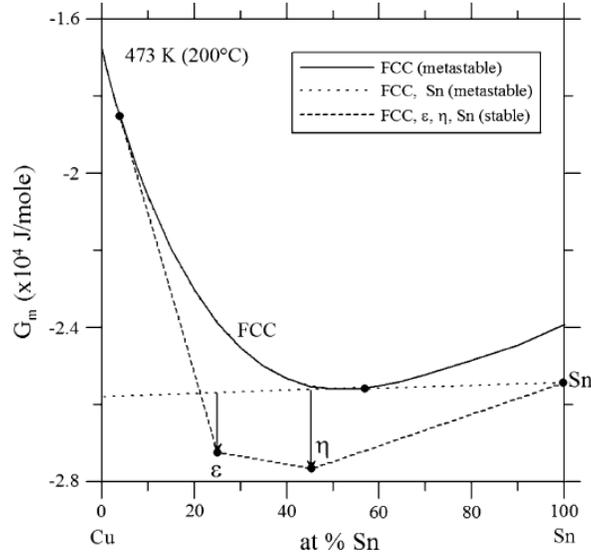
Figure 1: Free energy curve of Cu-Sn system vs. at. % Sn.[23] The arrows indicate the magnitude of the driving force for the nucleation of the Cu_6Sn_5 (η) and Cu_3Sn (ϵ) phases.

It is well-established that at some finite time after nucleation has occured, the Cu_6Sn_5 and Cu_3Sn phases grow at a constant parabolic growth rate.[21-23, 26, 27] Chao, et al., developed a parabolic model for growth of Cu_6Sn_5 and Cu_3Sn in a Cu-Sn couple at 150 °C which showed good agreement with experiments even at short anneal times (< 25 hours).[26] Thus, if the growth rate constant is known, the layer thickness for a given anneal time can be empirically determined. The relationship between the growth constant for a given phase, k; layer thickness, Δx; and anneal time, t, is given by the following equation:

$$k = \frac{\Delta x^2}{2t} \qquad (3)$$

The growth rate constant for a given IMC layer is mainly dependent on the interdiffusion flux in that layer as well as the interdiffusion flux in the adjacent IMC layer.[22] The Cu_6Sn_5 and Cu_3Sn phases will grow outwards into the Sn and Cu layers, respectively.[22] At the interface between Cu_6Sn_5 and Cu_3Sn, the phases grow but then consume each other with a net interfacial movement towards the Cu_3Sn side.[23] This can be schematically illustrated in Figure 2, from Kumar, et al.[22] There is an intrinsic diffusion flux of Cu towards the Sn side and of Sn towards the Cu side.[22] For a given anneal time, the Cu_6Sn_5/Sn interface is seen to move further than the Cu_6Sn_5/Cu_3Sn interface (see Fig. 2).[22]

8
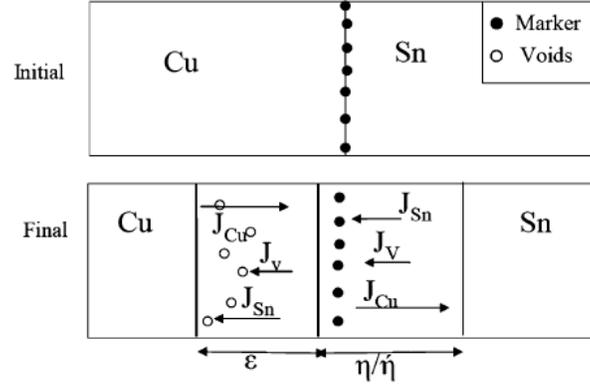
Figure 2: Schematic illustration of diffusion fluxes in Cu-Sn couple showing growth of the Cu_6Sn_5 (η) and Cu_3Sn (ε) IMC phases and interfacial movement.[22]

We have used Eq. (3) to model the expected layer thickness for Cu_6Sn_5 and Cu_3Sn in a Cu-Sn couple as a function of anneal time. The values for the parabolic growth rate constant, k, were taken from previous studies performed at 200 °C.[21-23] These values ranged from $7.2x10^{-17}$ to $1.6x10^{-16}$ m^2/s for Cu_6Sn_5 and $2.0x10^{-17}$ to $5.0x10^{-17}$ m^2/s for Cu_3Sn. The results of the calculations are presented in Figure 3. The deviation in modeled layer thickness values between the studies stems from the differences in k values, as they were empirically determined. Difficulties in measuring accurate IMC layer thickness, due to the thin nature of the layers and uneven interfaces, contribute to discrepancies between experimentally-determined k values.[21] Variations in grain size of samples in different studies can affect the contribution of grain boundary diffusion to IMC growth; however, it is difficult to quantify and compare this effect due to the continuous change in grain size as the layers grow.[23] There also may have been slight variations in experimental conditions.
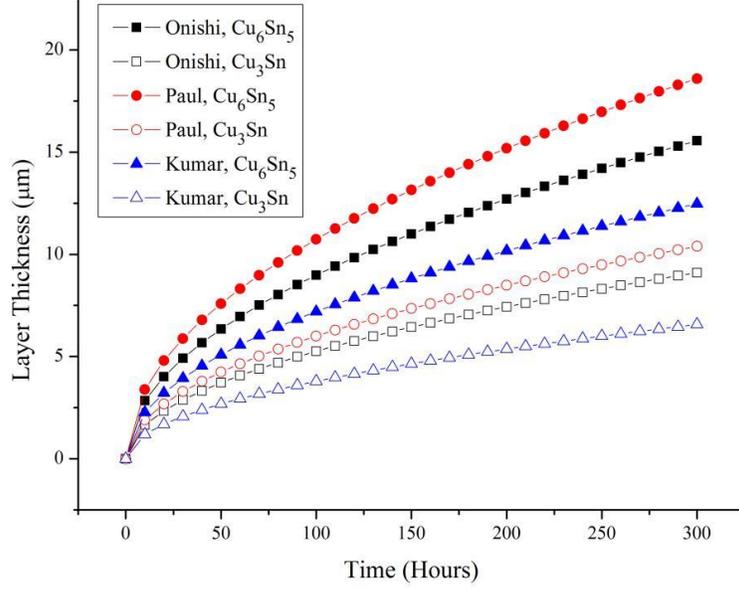
9

Figure 3: Growth rates for Cu_6Sn_5 and Cu_3Sn IMC layers from Eq. (3) using data from studies as listed in the legend.

The overall movement of each interface (Cu/Cu_3Sn, Cu_3Sn/Cu_6Sn_5, and Cu_6Sn_5/Sn) after initiation of growth is dependent on the square root of time and can be predicted using the following interfacial position function:[24, 28]

$$\xi_{ij} = 2\gamma_i\sqrt{\tilde{D_i}t} \tag{4}$$

In this equation, ξ_{ij} is the position of the interface between phase i and phase j, $\tilde{D}_i$ is the interdiffusion coefficient of phase i, t is time, and γ_i is a constant based on the ratio of the interdiffusion coefficients for each phase, $R_{ij} = \tilde{D}_i/\tilde{D}_j$. These values are readily available in the literature for our anneal temperature of interest.[21-24]

We will use this relationship in Eq. (4) to determine the appropriate anneal time for our Cu-Sn anodes based on the deposited thicknesses of Cu and Sn. Specifically, we want to ensure that we consume all of the deposited Sn so that we will theoretically have a layer of exposed Cu_6Sn_5 at the anode surface. Therefore, for a given initial thickness of Sn, we want the interface between the Cu_6Sn_5 and Sn layers to move by that same distance, since Cu_6Sn_5 is expected to grow into Sn. It is assumed that both IMC layers begin growing at the junction with Cu and Sn immediately. We have used values from Mei, et al., to plot the necessary anneal time at 200 ℃ versus deposited Sn layer thickness, which is analogous to $\xi_{Cu6Sn5/Sn}$ (Figure 4).[24]
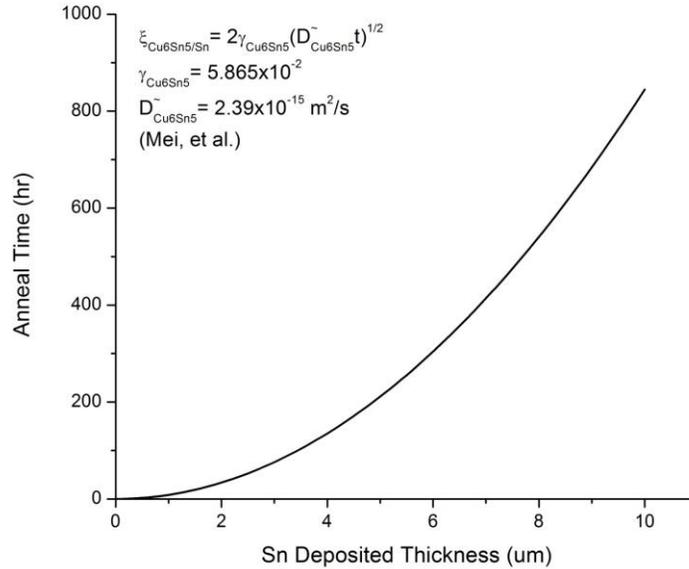
10

Figure 4: Necessary anneal time at 200 ºC for given Sn deposited thickness determined using Eq. (4) and corresponding values from Mei, et al.[24]

V. Technical Approach – Prototyping:

Electrodeposition of Sn:

Electrodeposition is a method of depositing metal onto a conductive surface submerged in a solution containing ions of the metal to be deposited.[29] The mass of deposited metal can be calculated by Faraday's Law of electrolysis,

$$m = \frac{Ita}{nF} \tag{5}$$

Where m is the mass reacted (deposited), I is the current, t is the time, a is the molar mass, n is the number of charges (electrons) exchanged (2 in our case), and F is Faraday's constant.[30] Rearranging the equation gives:

$$t = \frac{NnF}{I} \tag{6}$$

Where N is the number of moles deposited.[30] The required number of moles of Sn was obtained by multiplying the number of moles of Cu substrate by the desired Sn/Cu ratio (5/6 for Cu_6Sn_5). Using this formula, we decided on an applied current of 5.0mA, giving us a reasonably short deposition time of 1 hour 6 minutes, while still not having the current be so high as to result in an extremely uneven Sn layer.

Our electrodeposition bath is an aqueous solution consisting of 0.014M Sn(II) Sulfate, 1.93M methanesulfonic acid, and 0.05M hydroquinone.[31] We utilized methanesulfonic acid rather than sulfuric acid or just water as we had originally considered, due to several advantages that methanesulfonic acid provides. The use of methanesulfonic acid allows for a higher solubility of the metal salt (Sn Sulfate) in the solution than other common acids, and helps stabilize metal ions (particularly Sn(II) ions) against oxidation.[32] The oxidation of the Sn(II) ions to Sn(IV) ions

results in the formation of insoluble Sn salts, removing Sn from the solution and impeding the electrodeposition. Thus, the ability to slow this process is a very useful property. In addition, methanesulfonic acid solutions have a good electrical conductivity, aiding in the electrodeposition process.[32] As a 'natural acid', methanesulfonic acid is more environmentally friendly than other common acids such as sulfuric acid and hydrofluoric acid, producing fewer toxic reaction products and easily biodegrading.[32]

While methanesulfonic acid has an anti-oxidation effect, it alone is not sufficient to prevent the Sn(II) ions from oxidizing for very long. Using only methanesulfonic acid, the solution tends to oxidize and become ineffective after 2 hours.[33] However, the addition of a small amount of hydroquinone greatly slows the oxidation of the Sn ions, allowing the solution to remain useful for much longer, as the following figure 6 shows.[31] Figure 5 plots the percent decrease in the limiting current density j_L of the Sn(II) Sulfate solution with storage time for various hydroquinone concentrations. The limiting current density determines the deposition rate, as it is the maximum number of electrons that can flow per substrate area to reduce the Sn ions from solution to plate it.[31]
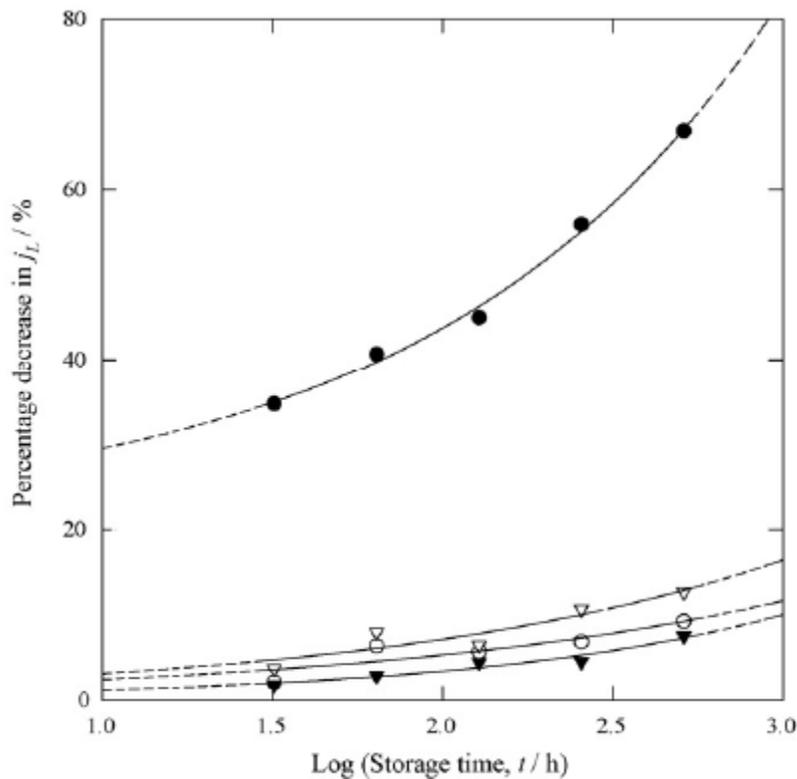

Figure 5: Decrease in limiting current density with storage time for hydroquinone concentrations of (●) 0.0M, (○) 0.005M, (▼) 0.05M, (∆) 0.5M.[31]

The electrolyte is prepared by adding 0.601g SnSO$_4$ (Sigma Aldrich) and 1.101g hydroquinone powder (Sigma Aldrich) to 200mL deionized water in a 400mL beaker.   37.098g methanesulfonic acid (Sigma Aldrich) is added to the solution while stirring in a fume hood. A

stir bar is added to the beaker and the solution stirred at the lowest setting until cool. If bubbles are present on the stir bar, the solution should be degassed in a bath sonicator.[33]

Cu foil substrates are secured to a glass backing with vinyl electroplating tape (3M). The tape is patterned to expose a 1.0 cm^2 area of Cu to the electrolyte, as shown in Figure 6a. The small sliver of exposed Cu is necessary to provide electrical contact between the Cu foil and potentiostat wires. The Cu foil serves as the cathode and is connected to the positive lead, and a Pt foil anode is connected to the negative lead. Both electrodes are lowered into the electrolyte, making sure to avoid contact between the leads and the electrolyte. The setup is illustrated in Figure 6b. The clips holding the electrodes are connected to the potentiostat via the red and blue clamps. A constant current of 5.0mA is applied between the electrodes for the prescribed time.
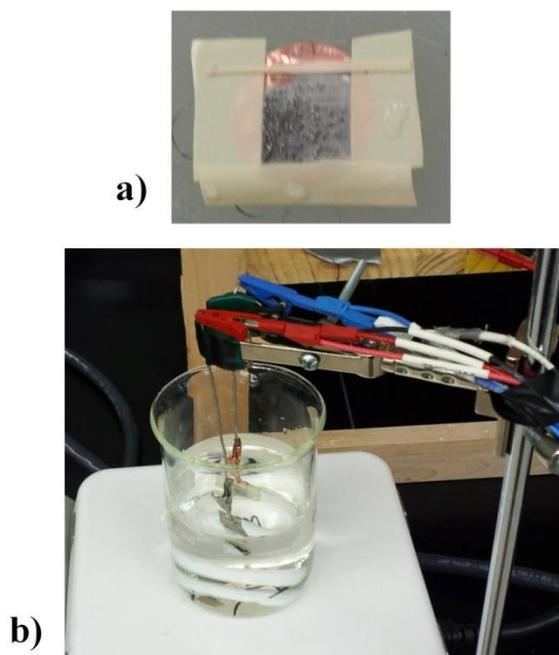

Figure 6: The electrodeposition setup is illustrated here. In a), the Cu foil substrate is attached to a glass backing via electrodeposition tape. The deposition occurs over a 1 cm2 area. The exposed foil at the top connected the substrate to the setup in b). The Cu and Pt electrodes are lowered into the electrolyte on a stir plate set at the lowest setting. The platinum electrode connects to the red wire (anode), and Cu to the blue (positive).

After deposition, the electrodes are removed from the apparatus and rinsed with deionized water. The Cu foil square is cut from the glass substrate and dried in a vacuum oven for ten minutes to evaporate any residual water. The samples are then weighed to determine the amount of Sn deposited.

Scanning Electron Microscopy:

XRD identifies the phases present in our anode, but does not necessarily correlate stoichiometry with the phases. Thus, we need a method of identifying the composition of the different phases in

each anode for comparison. We will use backscattered electron (BSE) imaging in SEM to observe the different Cu-Sn layers in a cross-section of one of our annealed anodes. This method should provide us with excellent contrast due to the inherent stoichiometric differences between the phases. We can then take advantage of the stoichiometric differences to verify each phase with energy dispersive x-ray spectroscopy (EDS). The individual phases should have a certain percentage of Cu (or Sn) and we can make an educated guess as to which phase is which based on its composition. This approach has been utilized in previous studies.[22, 23] The techniques required to prepare the samples are readily available in the literature.[22, 23, 34]

The BSE imaging mode in an SEM is able to provide phase contrast because the intensity of the backscattered signal is dependent on the atomic number, or Z, of the elements in the material of interest.[35] Incident electrons interacting with higher Z elements have a much greater probability of being elastically scattered back towards the detector.[35] Thus, phases containing these elements will show up relatively brighter. This probability is proportional to Z^2, so elements such as Cu ($Z = 29$) and Sn ($Z = 50$) will have good contrast.[35] In turn, the corresponding Cu_6Sn_5 and Cu_3Sn IMCs, due to the varying ratio of Cu and Sn in each, will be easily distinguishable under the correct SEM operating conditions.

Once a good BSE image is obtained and the individual phases are differentiated, EDS can be used to analyze the composition of each phase. When the electrons from the SEM gun hit the sample, there is a finite chance that an electron in a core shell of an atom will be excited to a higher energy level or ejected.[35] Another electron from a higher energy shell will subsequently relax and fill the hole that was left by the excited or ejected electron. This process generates the release of a photon, usually in the x-ray range, that has a certain energy that is characteristic to the element.[35] These x-rays reach a detector, typically made of p-type and n-type Si spaced out by a central region with diffused Li, and each produces a number of electron-hole pairs proportional to its energy.[35] An applied bias forms these electron-hole pairs into a charge pulse which is converted into a voltage signal by a field-effect transistor amplifier.[35] This signal is then converted into a signal pulse that has a height proportional to the x-ray energy.[35] Further processing and digitization allows the number of pulses, and thus photon count, for a given energy to be plotted over a spectrum.

A quantitative estimate of the concentration ratios of elements present in a given phase can be accomplished by determining the total number of characteristic x-rays counted for each peak of an element.[35] Any background needs to be subtracted. These steps can be completed using EDS system software. However, the direct ratios of peak areas for given elements is not directly equivalent to the ratios of elemental concentrations because different elements emit x-rays with varying efficiency.[35] In an SEM, a process called ZAF correction can be used to account for atomic number (Z), x-ray absorption (A), and x-ray fluorescence (F) factors.[35] This step can be performed using a software program on the computer handling the EDS data.[35] Thus, it is possible to obtain an accurate quantitative analysis of phase composition. For comparison, EDS scans can be performed along a line perpendicular to the layers in our anode.

Electrochemical Characterization Techniques:

Two electrochemical characterization techniques commonly used for battery research include electrochemical impedance spectroscopy (EIS), and galvanostatic cycling.[33] In the most basic form, the equipment used to perform these techniques is a potentiostat.[36] Potentiostats allow the

researcher to control the voltage or current applied to a working electrode/counter electrode system. Typically, a function generator maintains a potential difference between the two electrodes and the current is measured.[36] Conversely, potentiostats can also apply a variable current to maintain a specified voltage. Either alternating current (AC) or direct current (DC) signals are able to be applied to the system. Impedance data is also obtained from a potentiostat.[36]

EIS is an AC technique that measures the impedance of a system with respect to the frequency of the applied signal.[36] Results are typically presented in a Nyquist diagram, which plots imaginary impedance Z_{im} and real impedance Z_{Rc} at each frequency ω. The components of the impedance are determined from the equivalent circuit of the half-cell, and the most common equivalent circuit is the Randles circuit (Figure 7).[36]
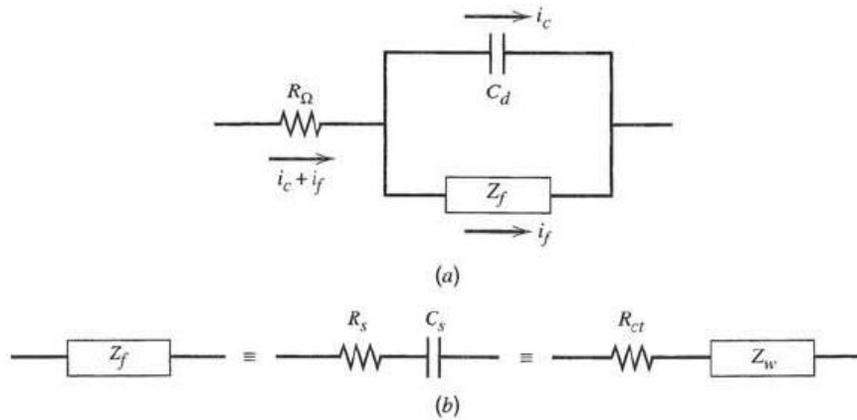
Figure 7: Equivalent circuit of a battery half cell (a). The Faradaic component is split into the charge transfer and Warburg impedance elements in (b).[36]

R_Ω represents the resistance of the whole cell, and the parallel component divides the impedance through the electrode/electrolyte interface into Faradaic and double layer components.[36] The Faradaic impedance Z_f is further divided into a charge transfer and mass transfer resistance (R_{ct} and Z_w, respectively). The mass transfer resistance is also known as the Warburg impedance. Evaluation of the Randles circuit at the high and low frequency limits reveal the shape of the Nyquist curve (Figure 8).[36] At high frequencies, the Nyquist curve takes the shape of a semicircle, with the semicircle diameter equal to R_{ct} and the leftmost intercept of the circle with the Z_{Rc} axis equal to R_Ω. The low frequency region of the curve is the mass transfer limited region and the frequency dependence comes from the Warburg elements, i.e. the impedance is due to diffusion.[36]
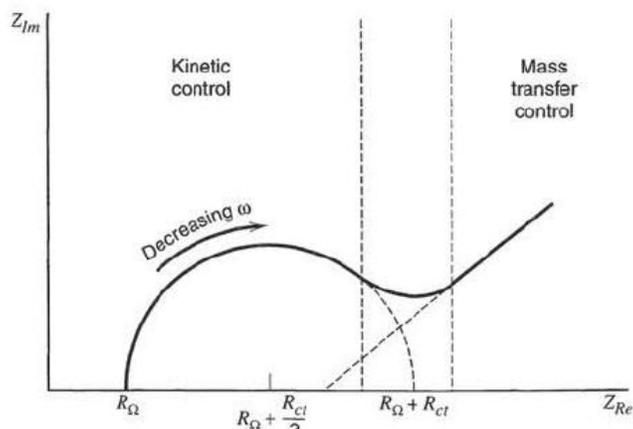
Figure 8: Typical EIS plot showing the high frequency semicircle followed by low frequency Warburg tail.[36]

Galvanostatic cycling is an electrochemical technique that is used to evaluate the lifetime of a half-cell or full-cell battery. The sample is charged and discharged with a fixed current rate called the "C-rate" and defined by C/R, where R is the number of hours for each charge or discharge cycle.[37, 38] C is expressed in amp-hours (Ah) and is calculated by multiplying the theoretical capacity of the alloy (Ah/kg) by the mass of the active material (kg).[33, 38]

In the galvanostatic cycling technique, the cell is repeatedly charged and discharged to set voltages at the specified C-rate.[37] The results are displayed in a voltage vs. time plot.[37] Several characteristics of the sample can be extracted from the data. Voltage plateaus correspond to two phase regions, and sharp voltage drops correspond to single phase regions.[38] The voltage drops correspond to current peaks in the cyclic voltammograms for the same electrode system.[36] The actual capacity of each half cycle is calculated from the cycling data within the testing equipment software.[33] The ratio of charge capacity to discharge capacity of each cycle is known as the coulombic efficiency and is unity for completely reversible systems. Several factors, including anode decrepitation, side reactions, and the formation of a solid electrolyte interphase (SEI) can reduce the columbic efficiency as irreversible capacity losses. These losses ultimately determine the cycle life of the battery.[5]

Half Cell Assembly:

The electrochemical performance of the deposited films will be evaluated using standard battery testing techniques. The first step is to assemble half cells using the deposited film and substrate as the working electrode and solid Na metal as the counter/reference electrode. All battery assembly will be carried out in an argon filled Vigor glovebox in the lab of Dr. Hu. The half-cell assembly feature is as follows:[33]

1. Place the top half of an MTI 304 Stainless Steel CR2032 button cell with O-ring case upside down on the battery assembly platform.
2. Insert the working electrode, face up.
3. Place two (2) Celgard Monolayer Polyethylene (PE) separators on top of the deposited film.
4. Drop 5 drops of 1M $NaPF_6$ in EC:DEC electrolyte into the cell.

16

5. Slice a thin piece of Na metal using a razor blade. Ensure that the Na is large enough to completely cover the working electrode surface area.
6. Place the Na metal on top of the separator and line it up with the working electrode.
7. Add one (1) MTI 316 Stainless Steel CR2032 Spacer.
8. Place an MTI 316 Stainless Steel CR2032 Wave Spring on top of the spacers.
9. Cap the cell with the other half of the MTI button cell, marked with an (+) and compress using tweezers.
10. Place the half-cell into an MTI MSK110-D Press with Crimping Die and press to 750 psi.
11. Remove the half-cell from the press and glovebox for electrochemical characterization.

We will primarily utilize EIS at open circuit voltage (OCV) to measure the resistance of the total half-cell. Low cell resistance is an indication of a correctly assembled half-cell.[33] EIS is typically performed first, as it is a non-destructive technique.[33] We will cycle our half cells to failure at a low C-rate (C/10 or less) and report the capacity and coulombic efficiency as a function of cycle number.

VI. Intellectual Merit, Broader Impacts, and Ethics:

Intellectual Merit:

There are several aspects to this project that may be considered novel. First, no studies have been reported about the use of η-Cu_6Sn_5 as a NIB anode, only the higher temperature (189C) η' phase.[8, 9] No mention of the stability of maintaining this phase was made in the literature, and it may be that after extended cycling there is an allotropic phase transformation from the η' to the η phase.[9] Therefore it was important to determine if this phase is electrochemically active with respect to sodium both theoretically and experimentally. Our first principles calculations determined that sodium can insert into η-Cu_6Sn_5 with a capacity of at least 82 Ah/kg, and volume relaxation of this structure identified many new areas for potential Na insertion. We applied kinetic growth models, developed previously from experimental and computational results, to design and prototype a working anode; however we were unsuccessful in tailoring the correct Cu-Sn ratio. In the end, we determined that η-Cu_6Sn_5 can act as a potential anode for sodium ion batteries, and that scalable processes such as electrodeposition may be used to produce this phase as long as the correct Cu-Sn ratio is achieved. As students, we became familiar with computational DFT software, alloy design and fabrication, and electrochemical testing.

Broader Impact:

Our results provide other researchers with a motivation to fabricate and test an η-Cu_6Sn_5 anode for NIBs. This anode, if resistant to volume cycling, will help to improve the lifetime of NIBs for grid scale storage. Additional techniques to improve the cycling life, such as anode patterning at the micron or nanometer scale, may also be explored. At the very least, future experimental results may inspire other researchers to investigate other alloy anodes for sodium ion batteries. Development of cheap, long term grid scale storage will provide for the incorporation of renewable energy technologies and reduce our dependence on fossil fuels. NIB technology exists solely at the research level; inspiring more research in the field can expedite the development of long lasting batteries.

17

Ethics and Environmental Impact:

Development of grid scale storage technologies is crucial to developing an all renewable energy infrastructure.[1] Reducing our dependence on fossil fuels will slow CO_2 production and reduce increases to the global temperature.[1] In regards to our system, sodium and to a lesser degree copper and tin are all earth-abundant elements and relatively easy to obtain in large quantities.[39] These materials could easily be recycled at the end of the battery cycle life to produce fresh anodes.

In addition to pure sodium, copper, and tin, we used methanesulfonic acid, hydroquinone, tin(II) sulfate, and 1M $NaPF_6$ in EC:DEC in our prototype fabrication. Dr. Hu's group had previously mixed the 1M $NaPF_6$ in EC:DEC electrolyte in an argon glovebox and it was handled entirely in this environment. All metallic sodium was handled and disposed of in the glovebox as well to prevent exothermic reactions from occurring in the presence of water. In total, we made about 600mL of electrodeposition electrolyte containing methanesulfonic acid, hydroquinone, and $SnSO_4$ in amounts outlined in Section V. Per the MSDS, the electrolyte was prepared in a fume hood while wearing lab coats, safety goggles, and nitrile gloves. The liquid methanesulfonic acid is stored in a chemical cabinet and the hydroquinone and $SnSO_4$ in a desiccator under vacuum. The environmental benefits of methanesulfonic acid are discussed in section V. All electrolyte was disposed of in an acid waste container and the amount and molarity of the electrolyte recorded.

VII. Results and Discussion:

First Principles Calculations:

The main goal of the modeling is to prove the insertion of Na atoms is energetically favorable. As mentioned earlier, we know that the insertion of Na into the $Cu_{12}Sn_{10}$ unit cell is favorable if the sodiation voltage is positive.[20] In order to determine the voltage associated with sodiation, we need to determine the energy of the $Cu_{12}Sn_{10}$ unit cell, the energy of the Na atom, and the energy of the sodiated $Cu_{12}Sn_{10}$ structure.[19]

The first step in calculating the total energy of the monoclinic $Cu_{12}Sn_{10}$ unit cell was to determine the optimized 'a' lattice constant and c/a ratio that produced the most energetically favorable cell. We carried out a manual relaxation for the $Cu_{12}Sn_{10}$ structure by varying the 'a' lattice constant (identical to 'b' lattice constant) and the c/a ratio. We selected four different lattice constants, 6.61, 6.66 (theoretical value), 6.71, 6.76 (Angstroms) and four different c/a ratios, 1.44, 1.49 (theoretical value), 1.54, and 1.59. [13-15] We ran the relaxation for all 16 possible data points and we observed a local minimum between the combination of 6.6-6.71 Angstroms and 1.49-1.54.

After completing the relaxations, we copied the CONTCAR output file to the POSCAR input file. The CONTCAR file describes the position of the atoms after the last step of the relaxation and the bulk energy calculation is taken of the relaxed structure.[12] We used the updated POSCAR file and the bulk energy INCAR file to obtain the bulk energy values for the specific lattice constants and c/a ratios.

The 16 bulk energy calculations for the different lattice constant and c/a ratio combinations are listed below in Table 4.

Table 4: Bulk energy table for Cu12Sn10 different combinations of 'a' lattice constant and c/a ratio.

Sorted Cu12Sn10 Bulk Energy Table				
	'a' lattice constant (Angstroms)	c/a ratio	Bulk Energy (eV)	c/a ratio
Max Energy (eV)	6.76	1.59	-8.24511320E+01	1.59
	6.61	1.44	-8.28991830E+01	1.54
	6.71	1.59	-8.27767250E+01	1.49
	6.66	1.59	-8.30214990E+01	1.44
	6.76	1.54	-8.30230510E+01	
	6.61	1.59	-8.31890400E+01	
	6.66	1.44	-8.31940740E+01	
	6.71	1.54	-8.32457640E+01	
	6.76	1.49	-8.33573250E+01	
	6.71	1.44	-8.33607290E+01	
	6.66	1.54	-8.33810310E+01	
	6.61	1.49	-8.33876850E+01	
	6.76	1.44	-8.34217300E+01	
	6.61	1.54	-8.34249430E+01	
	6.71	1.49	-8.34620960E+01	
Min Energy (eV)	6.66	1.49	-8.34721070E+01	

To pinpoint the lattice parameter and c/a ratio of relaxed $Cu_{12}Sn_{10}$ structures with the lowest bulk energy, the energies calculated as a function of these values are fit to a surface using MATLAB. A second order polynomial in both lattice parameter and c/a ratio with the form:

$$f = a + bx + cy + dx^2 + gxy + hy^2 \qquad (3)$$

is used, where a, b, c, d, g, and h are the constant fitting parameters and x and y are the lattice parameter and c/a ratio, respectively. This equation is then solved for the structure with the lowest bulk energy. This approximates the most stable structure of the alloy to adjust further DFT calculations.[40] The fitted surface is presented below in Figure 9.
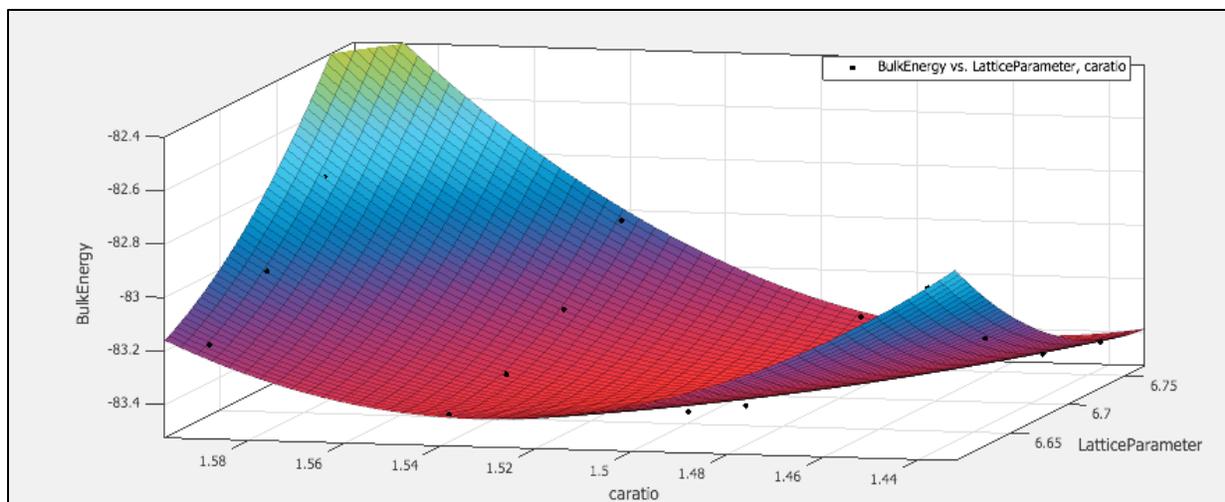
Figure 9: The second order surface which fit the 16 data points from Table 3.

From the fit surface, we determined the lattice constant and c/a ratio that yielded the ground state energy structure. The lattice constant is 6.68 Angstroms and the c/a ratio is 1.49. The goodness of the fit, reported as the r^2 value, is 0.9924. After calculating the optimized parameters from the fit, we performed a relaxation and bulk energy calculation using those parameters. The bulk energy calculation determined the minimum energy as -83.479 eV.

The next step after finding the ground state of $Cu_{12}Sn_{10}$ is to find the ground state energy of the Na atom. In order to do this, we relaxed the Na atom at its theoretical lattice constant of 3.633 Angstroms and then we calculated the bulk energy by following the same procedure used for the bulk energy of $Cu_{12}Sn_{10}$.[9-11] The bulk energy of the Na atom is -1.31 eV.

After finding the ground state energy of the Na atom we inserted Na into different interstitial sites, relaxed the cell, and ran a bulk energy calculation. We successfully inserted and relaxed 6 Na atoms into the optimized $Cu_{12}Sn_{10}$ structure (6.687 lattice parameter and 1.494 c/a ratio). For the insertion of the first Na atom we tried three different locations. The bulk energies for the three locations, seen below in Figure 10, were -83.26 eV, -83.29 eV, and -83.51 eV.

| Bulk E= -83.26 eV | Bulk E= -83.29 eV | Bulk E= -83.51 eV |
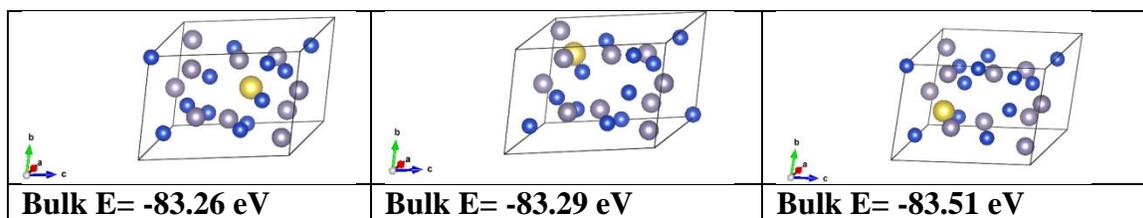
Figure 10: Three different locations for possible Na interstitials and the bulk energy for each structure. Blue atoms represent Cu, grey represents Sn, and yellow represents Na.

We used the lowest energy state to calculate the voltage for the 1 Na atom system. After inserting 1 atom, we estimated the next insertion site visually and let the ions relax by using the input parameter ISIF=2. The other insertion structures can be seen below in Figure 11.
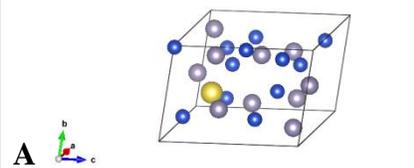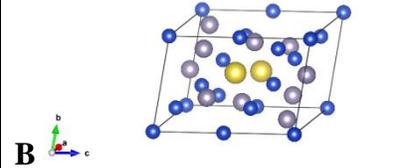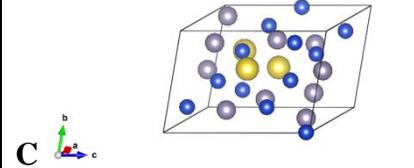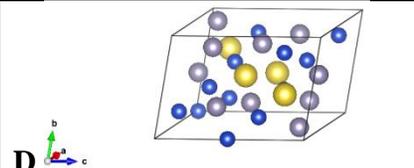
A	**B**	**C**
Bulk E= -83.51 eV	**Bulk E= -82.98 eV**	**Bulk E= -82.82 eV**
D	**E**	**F**
Bulk E= -81.95 eV	**Bulk E= -80.12 eV**	**Bulk E= -78.81 eV**
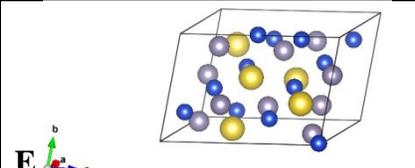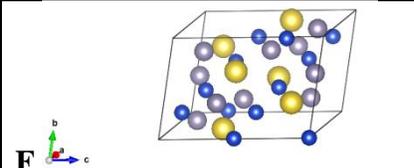
Figure 11: The unit cell for different concentrations (**A**-1 Na atom, **B**-2 Na atoms, **C**-3 Na atoms, **D**-4 Na atoms, **E**-5 Na atoms, **F**-6 Na atoms) of Na atoms and the bulk energy for each structure. Blue atoms represent Cu, grey represents Sn, and yellow represents Na.

After relaxing the ions in the unit cell, we calculated the bulk energy for each structure and they can be seen under the structure in Table 5. Once the bulk energies were calculated, we used equation 3 to determine the voltage associated with each degree of sodiation. The voltages can be seen in Table 5 and in Figure 12 is the voltage vs. Na concentration plot.

Table 5: The voltage associated with the insertion of each Na atom and all of the inputs to determine the sodiation voltage.

| Voltage (V)	Na-CuSn structure Bulk E (eV)	CuSn Bulk E (eV)	Na Bulk E (eV)	Faradays Constant	x (# Na atoms)
1.333341313	-83.505991	-83.478529	-1.3060866	96500	1
1.05676681	-82.980218	-83.478529	-1.3060866	96500	2
1.086226064	-82.819454	-83.478529	-1.3060866	96500	3
0.922578672	-81.945071	-83.478529	-1.3060866	96500	4
0.634645135	-80.121815	-83.478529	-1.3060866	96500	5
0.528127995	-78.81127	-83.478529	-1.3060866	96500	6
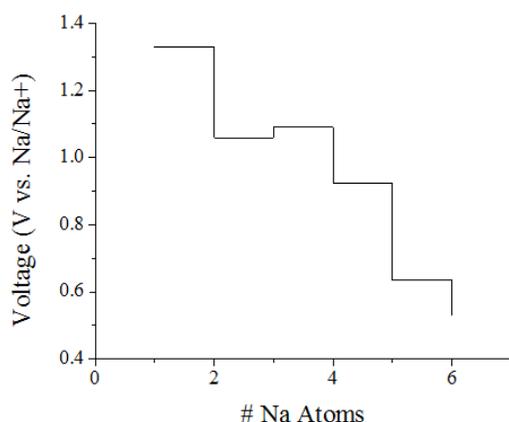
Figure 12: The voltage profile for different Na concentrations in the $Cu_{12}Sn_{10}$ optimized unit cell

The most important conclusion from the calculated sodiation voltages is that all of the voltages are positive; thus, the insertion of the Na atoms is energetically favorable.[20]

Except for a minor increase of 0.03 V between the second Na atom and third Na atom the voltage decreases as more Na atoms are inserted in the $Cu_{12}Sn_{10}$ unit cell. The decrease in voltage as Na concentration increases is the expected behavior; however, we do not have an experimental voltage profile to compare with the theoretical calculations.[2] We do not have an experimental voltage profile because we could not fabricate an anode of the desired Cu_6Sn_5 phase. The difficulties with the fabrication are discussed later in the report.

The insertion of Na atoms into the optimized $Cu_{12}Sn_{10}$ unit cell while the cell volume is constrained results in a large external pressure on the unit cell and it increases as the Na concentration increases, as seen in Table 6. The high pressure value indicates the cell is experiencing a large amount of stress at its current volume.[40]

Table 6: The external pressure for the Cu12Sn10 optimized unit cell due to each Na atom insertion. The pressure before and after volume relaxation are in the table.

x (# Na atoms)	Pressure (kBar)	Pressure After Relaxation (kBar)
0	-5.95	N/A
1	42.67	N/A
2	88.44	-12.14
3	135.04	N/A
4	182.58	N/A
5	241.29	N/A
6	299.04	-9.80

Due to the large pressure, we performed a cell volume relaxation to determine the theoretical volume expansion for two of the sodiated structures. We relaxed the cell volume for the structure with two Na atoms and six Na atoms. The two Na system corresponds with the $NaSn_5$

phase that is expected to form, and the six Na system is the unit cell with the highest capacity that we were able to relax.[9] The volume relaxations for the sodiated structures followed the same procedure as the relaxation for the $Cu_{12}Sn_{10}$ unit cell. For the 2 Na complex, we varied the lattice constant (6.6, 6.687, 6.8, 6.9 Angstroms) and the c/a ratio (1.4, 1.494, 1.59, 1.69, 1.79, 1.89) to build a 3-dimensional surface that consisted of 24 data points. The 24 data points can be seen below in Table 7.

Table 7: Bulk energy table for 2Na-Cu12Sn10 different combinations of 'a' lattice constant and c/a ratio.

Sorted Bulk Energy Table for Insertion of 2 Na Atoms				
	'a' lattice constant (Angstroms)	c/a ratio	Energy (eV)	c/a ratio
Max Energy (eV)	6.6	1.4	-78.949788	1.89
	6.687	1.4	-80.805869	1.79
	6.6	1.494	-81.873004	1.69
	6.8	1.4	-82.500182	1.59
	6.687	1.494	-82.98021	1.494
	6.9	1.89	-83.244676	1.4
	6.6	1.59	-83.358252	
	6.9	1.4	-83.425091	
	6.8	1.89	-83.760781	
	6.9	1.79	-83.832429	
	6.8	1.494	-83.845874	
	6.687	1.59	-83.993311	
	6.9	1.494	-84.165982	
	6.6	1.69	-84.22096	
	6.687	1.89	-84.223418	
	6.9	1.69	-84.262378	
	6.8	1.79	-84.289069	
	6.9	1.59	-84.362536	
	6.8	1.59	-84.369178	
	6.687	1.69	-84.510529	
	6.8	1.69	-84.523149	
	6.6	1.79	-84.564103	
Min Energy (eV)	6.687	1.79	-84.57107	

The surface is fit with a second order polynomial of the same form used for the $Cu_{12}Sn_{10}$ surface. The fit surface approximated that the ground state energy structure occurs with a lattice constant of 6.76 Angstroms and a c/a ratio of 1.72, as seen in Figure 13. The goodness of the fit, reported as the r^2 value, is 0.9664. After calculating the optimized parameters from the fit, we performed

a relaxation and bulk energy calculation using those parameters. The bulk energy calculation determined the minimum energy as -84.59 eV.
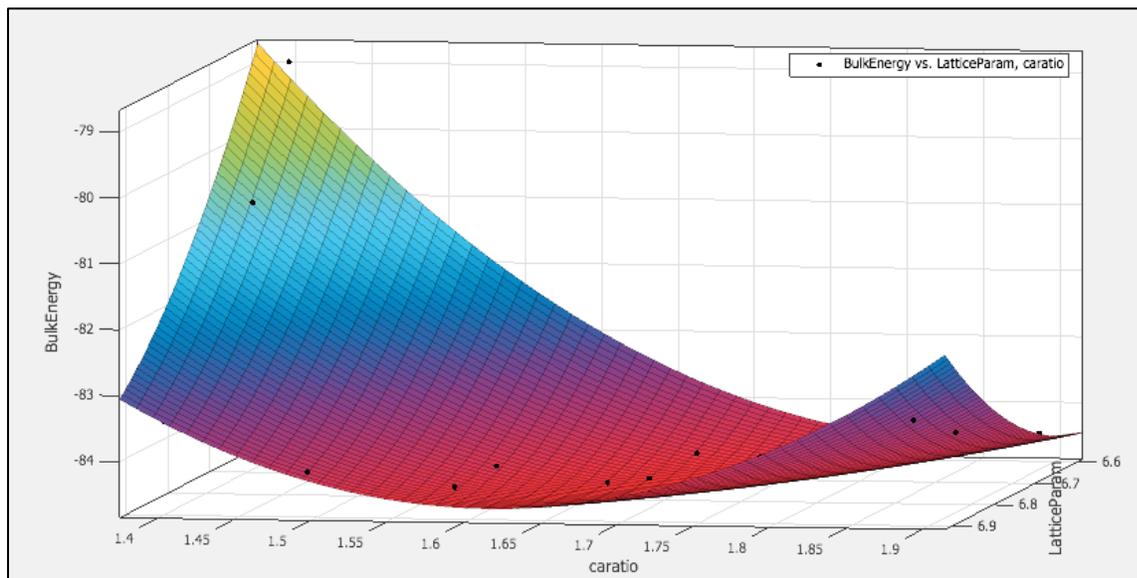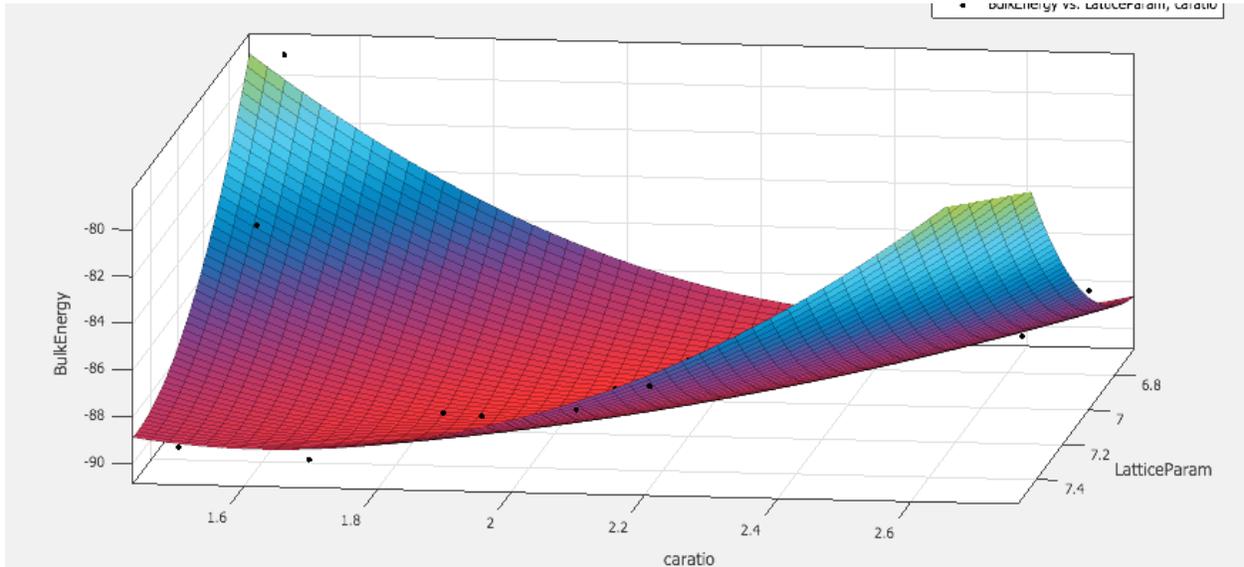

Figure 13: The second order surface which fit the 24 data points from Table 7.

The optimized lattice constant, 6.76 Angstroms, and c/a ratio, 1.72, yielded a volume expansion of 19.01%, while the theoretical volume expansion from Sn_2 to Na_2Sn_{10} is 30.14%.[13-15] This shows that less volume expansion is expected in the $Cu_{12}Sn_{10}$ cell than the Sn only cell, which was the goal of the inactive-active metal anode.

For the 6 Na atom structure, we followed the same relaxation procedure discussed for the $Cu_{12}Sn_{10}$ and $2Na-Cu_{12}Sn_{10}$ structure. The selected lattice parameters were 6.687, 6.9, 7.2, 7.5, to 7.8 Angstroms and the c/a ratios are 1.494, 1.69, 1.89, 2.09, 2.2, 2.5 (1 data point), and 2.7. Using the selected lattice parameters and c/a ratios we created a 3-dimensional surface consisting of 31 data points. The 31 data points can be seen below in Table 8.

Table 8: Bulk energy table for 6Na-Cu$_{12}$Sn$_{10}$ different combinations of 'a' lattice constant and c/a ratio.

	Sorted Na6-Cu12Sn10 Bulk Energy Table			
	a' lattice parameter (Angstroms)	c/a ratio	Energy (eV)	c/a ratio
Max Energy (eV)	6.687	1.494	-78.811714	2.7
	7.8	2.7	-80.797136	2.5
	7.5	2.7	-83.262893	2.2
	7.8	2.2	-84.343503	2.09
	6.9	1.494	-84.524308	1.89
	6.687	1.69	-85.482926	1.69
	7.2	2.7	-86.234366	1.494
	7.5	2.2	-86.501199	
	6.9	2.7	-87.137392	
	7.5	2.09	-87.571471	
	7.2	2.2	-87.602575	
	7.5	1.89	-87.847198	
	7.8	1.89	-88.017803	
	6.687	2.7	-88.114294	
	7.8	2.09	-88.373617	
	6.687	1.89	-88.378875	
	6.9	1.69	-88.582388	
	7.2	1.494	-88.599267	
	7.8	1.494	-88.726031	
	7.2	2.09	-88.92773	
	7.8	1.69	-89.375349	
	6.687	2.09	-89.464298	
	6.687	2.5	-89.545122	
	7.5	1.494	-89.551558	
	6.9	1.89	-89.646579	
	6.9	2.2	-89.795384	
	6.687	2.2	-89.813138	
	7.5	1.69	-89.963852	
	7.2	1.69	-90.126962	
	7.2	1.89	-90.211745	
Min Energy (eV)	6.9	2.09	-90.289417	

The fit surface approximated that the ground state energy structure is generated when the unit cell has a lattice constant of 7.03 Angstroms and a c/a ratio of 2.09, as seen in Figure 14. The goodness of the fit, reported as the r^2 value, is 0.8422. After calculating the optimized

parameters from the fit, we performed a relaxation and bulk energy calculation using those parameters. The bulk energy calculation determined the minimum energy as -89.52 eV.

Figure 14: The second order surface which fit the 31 data points from Table 8.

The volume of the optimized ground state structure, 7.03 Angstrom lattice constant and 2.09 c/a ratio, is 660.1 Angstroms^3. The expanded cell volume indicates a 62.60% volume expansion with respect to the $Cu_{12}Sn_{10}$ unit cell. The $6Na\text{-}Cu_{12}Sn_{10}$ is the most sodiated structure we proved with theoretical calculations. The $6Na\text{-}Cu_{12}Sn_{10}$ structure has the theoretical capacity of 82 Ah/kg, which was determined from equation 7 below.[38]

$$\text{Capacity} \left[\frac{\text{Ah}}{\text{kg}}\right] = \left(\frac{ze^-}{yA_m^{alloy}}\right) * F * \left(\frac{3600\text{kg}}{1000\text{hr}}\right) \tag{7}$$

Thus, our calculations indicate we can design a $\eta\text{-}Cu_6Sn_5$ anode that at the theoretically proven maximum sodiation, 6 Na atoms, will have the capacity of 82 Ah/kg and experience a volume expansion of 62.60%.

IMC Growth:

The initial plan for IMC growth was to deposit a stoichiometric amount of Sn to completely anneal a film of $\eta\text{-}Cu_6Sn_5$. The kinetic modeling in section IV indicated that annealing a film at least 20μm thick would take several days. As such, we focused on the interfacial movement model to design a deposition and annealing schedule that would completely transform the Sn layer to $\eta\text{-}Cu_6Sn_5$ in a reasonable amount of time. Initially, the thin Sn layer was electrodepositied; we found, however, that the film thickness was not uniform. A more conformal, 500 nm Sn layer was deposited onto a 1.0 μm Cu layer on doped-Si via physical vapor deposition and annealed for 2 hours and 7 minutes based on figure 4. This was done in the Fab Lab on the Temescal Electron Beam Deposition System and Metra Thermal Evaporator, respectively, with the help of Fab Lab staff member Tom Loughran. Deposition was measured by a Quartz crystal microbalance present in both machines. This system had the added benefit of easily being cleaved for cross-sectional analysis.

Electrodeposition:

When we deposited Sn via electrodeposition, we discovered that the amount of Sn deposited for a given time was less than that predicted by Faraday's Law of Electrolysis (see Table 9 below). There are several possible explanations for this discrepancy.

Table 9: Comparison of calculated Sn deposition versus measured Sn deposition.

Sample	Cu mass (g) (est.)	Desired Sn mass (g)	Deposition current (mA)	Deposition time (min)	Deposited Sn mass (g)
1	0.0091	0.0141	5.0	90	0.0134
3	0.0091	0.0141	5.0	66	0.0077
5	0.0093	0.0144	5.0	90	0.0117
6	0.0092	0.0143	5.0	90	0.0061
7	0.0076	0.0007	0.5	40	0.0001

The first possibility is experimental error. We originally cut out our Cu substrates as 16 mm diameter discs using a punch, which we weighed. We then used electroplating tape to cover the disc, reducing the deposition area to 1.0 cm^2. After the Sn was deposited, we cut out the square and weighed it. We approximated the mass of Cu in the 1.0 cm^2 by dividing the total mass of the original disc by its area to get an areal mass density. By this method, we got Cu masses of about 0.009 g. However, when we later weighed some cut out 1.0 cm^2 Cu squares, the measured mass was only about 0.0076 g. Since we got the amount of Sn on the sample by subtracting the approximated Cu mass from the total mass, this error in the Cu mass means that there was about 0.0014 g more Sn than we had originally thought there was. However, when using this more accurate value for the Cu mass to get the actual amount of Sn on the samples, the time required to deposit that much Sn is still less than what we deposited for.

The second possibility is oxidation of the Sn ions. The Faraday's Law equation above shows that the deposition time is directly proportional to the number of electrons that need to be exchanged (n).[30] If some of the Sn(II) ions in the solution oxidized to Sn(IV) ions, the effective *'n'* would increase, and thus the deposition time for a given mass of Sn would increase. However, given that our deposition times were about 1.3 times longer than what should have been required for the amount of Sn deposited, the effective *'n'* would have to be 2.7. This would require about 36% of the Sn(II) ions to have oxidized to Sn(IV), which would have resulted in significant discoloration and precipitation in the deposition solution, which we did not observe.[31, 41] Thus, the oxidation of the Sn ions could be a contributing factor, but it cannot be the only cause.

The third possibility relates to ion transport. Faraday's Law of Electrolysis only states how fast the reaction will take place if the reactants (Sn ions and electrons) are available. Given that the Sn ions are dispersed in solution, they must make their way to the cathode (Cu substrate) to be reduced and deposit out. If the diffusion of the Sn ions through the solution was slower than the electrolytic reaction, it would be the rate-limiting step, and would slow the deposition rate.[30] Since we used the same deposition solution for multiple samples, the depletion of Sn ions in the solution increases this effect, possibly explaining sample 6 which had only about half as much Sn as previous samples for the same deposition time. This could also explain the very large

voltages (~2.4 V) we observed during deposition, which were much larger than the EMF for the Sn reduction reaction.[30] If the Sn transport was slower than the reaction, un-reacted electrons would build up at the cathode (Cu substrate), waiting for Sn ions to react with. This build up of electrons polarizes the system, resulting in a higher potential difference (voltage).[30]

The final possibility is competing chemical reactions. During the electrodeposition we observed some bubbles forming on the sample, indicating that other reactions were taking place in the solution. The most likely reaction is the reduction of hydrogen ions into hydrogen gas, which is a common cathodic reaction.[30] These competing reactions would use up electrons which otherwise would have been used to reduce Sn ions from the solution. As a result, the Sn deposition current would effectively decrease as not all of the electrons are going to Sn ions, and the deposition rate would thus be less than predicted.

X-Ray Diffraction:

Our samples were examined at the UMD X-ray Crystallographic Center under Dr. Peter Zavalij, and were actually run by graduate student Kai Zhong on their XRD machine. The results are presented below:

Table 10: Phases identified via X-Ray Diffraction for various annealed samples.

Sample	Annealing time (hrs)	Sn	Cu	Cu_3Sn	Cu_6Sn_5
1	20	X	X	X	
3	20	X	X	X	X
5	20	X	X	X	X
6	20	X	X	X	X
1a	120	X	X	X	
3a	120	X	X	X	X
5a	120	X	X	X	
6a	120	X	X	X	X
6b	120	X			
7	12		X	X	
Si3 (Control)	0	X	X		
Si5	2.116		X	X	
Si6	2.116		X	X	

The sample diffractograms can be seen in Appendix A. All numbered samples were electrodeposited, and samples with the "Si" prefix in their name were the thermally evaporated

samples. Samples 1, 3, 5 and 6 are the same samples as 1a, 3a, 5a, and 6a, just annealed for a shorter time.

The electrodeposited samples were first annealed for 20 hours and we observed both Cu-Sn phases being present. However, when these samples were annealed for an additional 100 hours a curious result occurred: the Cu_6Sn_5 phase disappeared in two samples (1a, 5a) while having a significant reduction in peak intensity for the other two samples (3a, 6a). This went against the modeling data which suggested that the Cu_6Sn_5 phase was faster growing, and would overtake the Cu_3Sn phase. A rough surface layer was present on top of the electrodeposited film on top of what appeared to be the alloyed layer. Sample 6b was a powder sample scraped off of one of our films to observe if this rough surface had any phases present. As seen from the table, XRD confirmed our thought that the rough powder was just Sn that was not consumed.

For electrodeposited sample 7 and the thermally evaporated samples (excluding Si3) we annealed based on the growth modeling and had less than favorable results: all of the Sn was consumed, but only strong Cu_3Sn peaks were observed in the diffractograms. Si3, the control sample, showed only Sn and Cu peaks as expected.

The phase diagram for the Cu-Sn system shows that the Cu_3Sn and Cu_6Sn_5 phases exist in very small concentration ranges of about 1 wt. % Sn each.[8] At 200 ºC, there is a substantial two-phase region that exists between them. Thus, a likely cause of the preferred development of Cu_3Sn over Cu_6Sn_5 for longer annealing times would be that we simply had too little Sn deposited on our Cu substrates. The Cu_6Sn_5 phase was shown to form in greater amounts than Cu_3Sn for shorter annealing times. This occurrence agrees with the kinetic growth modeling and the characteristic of Cu_6Sn_5 having a larger initial thermodynamic driving force for formation.[23] However, if our composition put us in the two-phase region of Cu-Sn, then it is reasonable that for longer annealing times the thermodynamic stability would be pushed to the Cu_3Sn phase as Sn is consumed. This effect would be exacerbated for greater deviations from the necessary compositions of Cu and Sn.

The relatively small concentration range for Cu_6Sn_5, our desired phase, needs to be an additional consideration when trying to consume all of the Sn during annealing. A better method may be to deposit a given amount of Sn on the Cu substrates, anneal, and then perform XRD to analyze the phase constituency. If Cu_3Sn is more prevalent than Cu_6Sn_5, then the process should be repeated to deposit more Sn. This additional amount of Sn would hopefully shift the composition of the anode from the two-phase region towards the narrow Cu_6Sn_5 window.

Scanning Electron Microscopy/Energy Dispersive X-Ray Spectroscopy

Two combination SEM/EDS images are presented in Figure 15. The image on the left is of sample Si3, which was not annealed. A clear distinction between the Sn (green), Cu (blue), and Si (red) layers are observed. The image on the right is of sample Si5, which was annealed for 2 hours and 7 minutes. The green and blue layers have mixed, indicating that the Cu and Sn have interdiffused. XRD results of this sample reveal that only Cu and Cu_3Sn exist, all of the Sn has been annealed out. Combining these results with the BSE images below, we conclude that the entire Sn layer has been annealed out as predicted by the interfacial movement model.
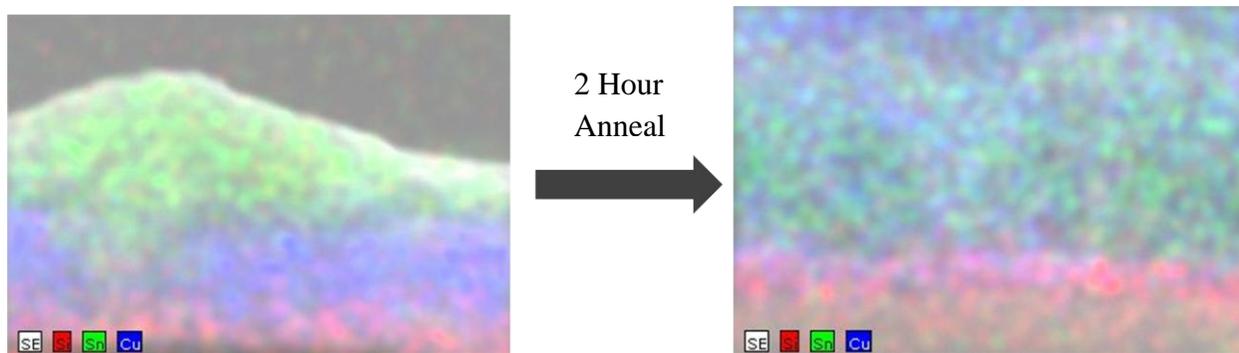
2 Hour Anneal

Figure 15: BSE images of a pristine (left) and annealed (right) CuSn couple on Si. After annealing, Cu appears to have diffused through the Sn layer. Layer thickness is approximately 1.5um.

Examining the BSE image of sample Si5 reveals that Sn and Cu appear to have annealed into the Si. This phenomenon is most likely an artifact of the interaction volume of the electron beam. An estimation of the interaction volume is given by the following equation:

$$\rho R = aE_0{}^r \tag{8}$$

Where ρ is the density of the chemical species, R the electron range, E the accelerating voltage in keV, and a a scaling factor of $10\mu g/cm^2$.[35] For a beam voltage of 15.0 keV and Cu_3Sn density of 8.88 g/cm^3, the interaction volume is 0.43 microns, or about one-third the total film thickness.[13-15, 35]

BSE images of the cross sectional areas were also taken to identify potential phases using phase contrast. An image of sample Si5 is presented below in Figure 15. No phase contrast is observed in the image, even though XRD reveals that both Cu and Cu_3Sn are present. In our analysis of the sample, however, we had trouble correcting the beam astigmatism which may have resulted in loss of good focus on the sample.
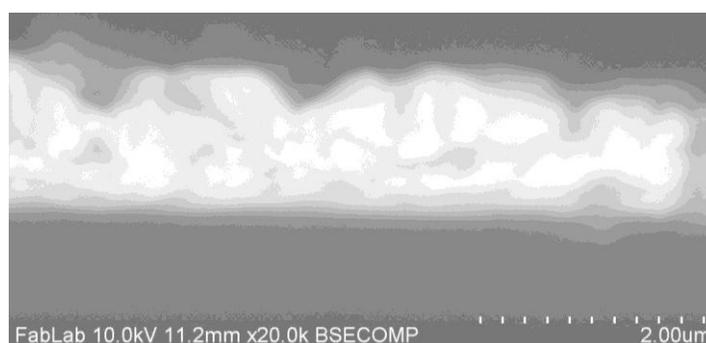
Figure 16: BSE image of the annealed Si5 sample. No phase contrast is observed.

Electrochemical Characterization:

Phase and composition analysis of the samples indicated that the desired η-Cu_6Sn_5 phase was not formed for our deposited and annealed anode samples. Electrochemical testing of the samples was still performed, however, to determine if the ε-Cu_3Sn phases exhibit reversible capacity and would warrant first principles analysis of the system. To do this, half-cells of both the electrodeposited and thermally evaporated samples were assembled according to the procedures outlined in section V. Each half-cell was characterized with EIS on a BioLogic VMP potentiostat; the frequency was varied from 100kHz to 100mHz and a total of 60 data points recorded. The initial R_Ω value was used to determine if the half-cell has good electronic conductivity and will be suitable for galvanostatic cycling. The charge transfer resistance was calculated from the diameter of a semicircular fit as outlined in section V. The fit was performed with the BioLogic VMP software. The EIS plots for 3 samples, Si3, Si6 and 7, before and after galvanostatic cycling are presented in Appendix B, and relevant values are reported below in Table 11. The EIS measurements after cycling for the other half cells were too noisy to accurately extrapolate any results.

Table 11: Resistance values extrapolated from EIS results for half-cells before and after cycling.

	Initial		After Cycling	
Sample	R_Ω **(ohm)**	R_{ct} **(ohm)**	R_Ω **(ohm)**	R_{ct} **(ohm)**
Si3 (control)	10.02	3093.98	72.04	7626.96
Si6	8.49	3618.52	3.42	5124.58
7	7.41	2826.52	78.72	2033.28

It is expected that the formation of a solid electrolyte interphase (SEI) layer will increase both R_Ω and R_{ct}. The SEI is an electronic insulator and increases the overall resistance of the cell, and the ionic conductivity of Na ions is less than through the liquid electrolyte.[42, 43] This behavior holds well for samples Si3 and Si6, but for sample 7, R_{ct} decreases after cycling. The EIS measurements before and after cycling were not taken at the same potential which can affect the impedance measurements.[36]

The half-cells were galvanostatically cycled between 1.5 and 0.005 V vs. Na/Na+ to evaluate the cycling performance. All samples were analyzed using an 8-channel MTI Battery Analyzer. The initial charge for each cell is from OCV to 0.005V vs. Na/Na+. Three annealed samples (7, Si5, and Si6) were cycled at C/20, and one (Si2) at C/100. A control sample that was not annealed (Si3) was also cycled at C/20 for comparison. Results of the galvanostatic cycling are presented below in Table 12.

Table 12: First cycle capacity and coulombic efficiency values for various half-cells.

Sample	C-Rate	Current (mA)	First Charge Capacity (mAh/g)	First Disharge Capacity (mAh/g)	Coulombic Efficiency (%)
Si3	C/20	0.0072	351.858	245.756	69.85
Si5	C/20	0.0073	35.185	4.056	11.53
Si6	C/20	0.0066	81.634	10.171	12.46
7	C/20	0.0042	321	18.922	5.89
Si1	C/100	0.0015	17.208	3.929	22.83
Si2	C/100	0.0029	40.288	4.035	10.02

All annealed samples exhibited an initial charge capacity ranging from 17.208 to 321.000 mAh/g. After this initial charge, however, the cycling capacity drops to values ranging from 4.035 to 18.922 mAh/g. The initial, irreversible capacity is likely due to the formation of an SEI layer; where the electrolyte decomposes at low voltage to form a passivating layer at the anode surface.[43] One indicator of SEI formation is the increase of R_{ct} in the impedance plots after cycling. The variation in initial capacities between the samples may be a result of variation in the surface roughness; larger roughness results in more area for electrolyte to decompose into SEI.[43] The control sample exhibited a much higher reversible discharge capacity than the annealed samples, although the capacity is less than the theoretical capacity of 847 mAh/g for Sn.[5] Baggetto, et al. reported that for the η'-Cu_6Sn_5 phase, Na alloys with Sn within a Cu matrix. As such, the voltage profile exhibited four plateaus corresponding to the theoretical Na-Sn voltage profile.[2, 9] We examined the voltage profiles of the control sample, Si3, and well as the annealed samples Si6 and Si2 to identify any alloying plateaus. Figure 17a is the voltage profile for the first charge-discharge cycle of sample Si3. The first charge cycle exhibits two plateaus at about 0.35 and 0.25V vs. Na/Na+, and the discharge profile exhibits four plateaus at 0.25, 0.39, 1.00, and 1.12V vs. Na/Na+. These are in reasonable agreement with theoretical plateaus at 0.15, 0.17, 0.45 and 0.7V vs. Na/Na+ which do not take into account overpotentials due to Na kinetics.[2] The voltage profiles for samples Si2 and Si6, presented in Figure 17b and 17c, respectively, show no plateaus and as such exhibit capacitor-like behavior.
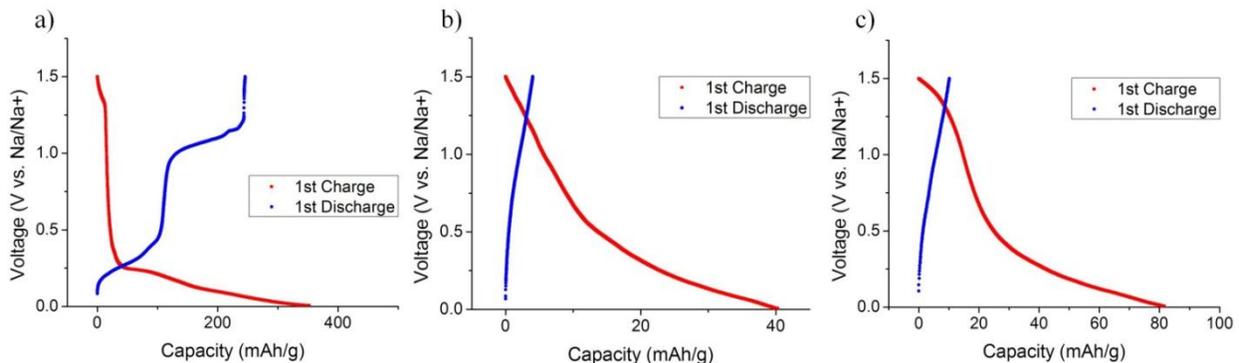
Figure 17: First cycle voltage profiles for a) Si3 (control), b) Si2 (cycled at C/100), and c) Si6 (cycled at C/20).

The cycling behavior of the three half-cells is presented in Figure 18. The capacity of sample Si3 (figure 18a) slowly fades for the first 9 cycles before rapidly decreasing to a value of about 4 mAh/g. This behavior is typical of Sn film anodes, which experience pulverization due to extreme volume expansion upon charging.[2, 44] Both sample Si2 and Si6 exhibit an immediate decrease in capacity after the first charge cycle and continue to cycle at this capacity for >20 cycles.
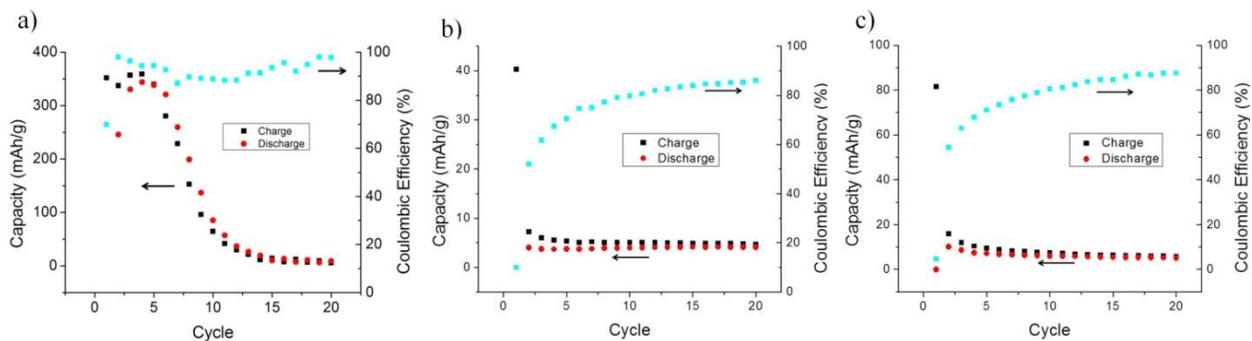
Figure 18: Cycling behavior for a) Si3 (control sample), b) Si2 (cycled at C/100), and c) Si6 (cycled at C/20). Only Si3 exhibits a reasonable reversible capacity.

VIII. Conclusions:

Our first principles calculations indicate that Na can insert into η-Cu_6Sn_5 with a capacity of at least 82 Ah/kg with a volume expansion of 62.6%. This capacity is less than that reported for carbonaceous anodes, however many more interstitial sites opened up when the 6 Na atom system was allowed to relax.[45] For the 2 Na atom system the associated volume change is 19.01%, about 10% less than the volume change from Sn to $NaSn_5$, the first alloy formed for pure Sn anodes. This metric suggests that the η-Cu_6Sn_5 phase may have improved lifetime over Sn anodes due to less volume expansion associated pulverization. Further prototyping and characterization is required to test our first principles calculations experimentally.

IX. Future Work:

There is much work left to be done to fully understand the CuSn system for NIBs. Baggetto et al. completed an analysis of the diffusion of Na atoms along different pathways in both the high and low temperature Cu_6Sn_5 phases.[9] By measuring the required jump distance for Na atoms diffusing in a zig-zag path along the c axis and the path formed by tunnels of Sn atoms, Baggetto et al. estimate that the latter is energetically more favorable without considering the size of the channel.[9] We suspect that the activation energy of diffusion along this path can be modeled by computing the bulk energy of the structure with Na atoms at different positions along the path. The resulting energies of these structures outlines an energy barrier for diffusion of Na atoms. The height of this barrier is the activation energy of moving an Na atom from one interstitial site to the next along this pathway. If this activation energy can be used to calculate the potential of Na intercalation, it would provide insight into the efficacy of Cu_6Sn_5 as an anode material.[9]
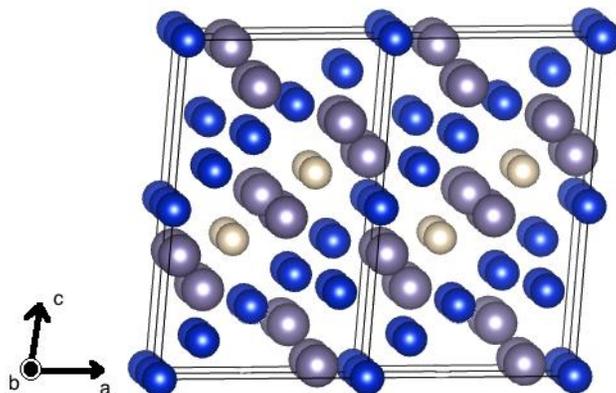
Figure 19: Projection with slight rotation along the [010] direction.[9] Na atoms (tan) have been placed in a potential interstitial site between Sn atoms (silver). Cu atoms are shown in blue.

The most favorable diffusion pathway of Na into and through the $Cu_{12}Sn_{10}$ structure can be determined from the Na insertion sites calculated previously. A method known as the nudged elastic band (NEB) method is a way to calculate the minimum energy pathway (MEP) between an initial and final energy state using density functional theory.[46, 47] This method has been used to investigate lithium diffusion in V_2O_5 cathodes for lithium ion batteries.[47] Three potential diffusion pathways of Li through V_2O_5 were examined in this work, and the pathway with the lowest activation energy barrier to diffusion is predicted as the probable pathway for Li diffusion.

In the NEB method, a series of 4 to 20 images or replicas of the transition from the initial to final state are used to calculate the MEP. Continuity between the images is maintained by adding a spring interaction between the images that mimics an elastic band.[46] The MEP is derived from this band by an optimization that minimizes forces acting on the band.[46] The activation barrier of the transition is given by the energy of the highest saddle point in the MEP.[46] In our case, time permitting, we will use the NEB method to trace the diffusion of Na through various pathways in η-Cu_6Sn_5 and determine the lowest energy diffusion pathway, similar to the work of Ma, et al.[47]

Along with the nudged elastic band calculation, we would like to explore the insertion of more Na atoms in η-Cu_6Sn_5 and determine the volume expansion experienced for the other sodiated structures. Also, we would like to perform first principle calculations, similar to the calculations done for η-Cu_6Sn_5, for ε-Cu_3Sn to compare to our experimental results.

Optimization of the alloy fabrication method will allow us to test half-cells of the desired phase. Iterative deposition and annealing, as well as sputtering or pulsed laser deposition, could be used to fabricate the correct phase for testing in the same half-cell configuration outlined above.

X. Acknowledgements:

Appendix A: X-Ray Diffractograms:

Reference Diffractograms:

Cu_6Sn_5:[7, 13, 14]

Cu₃Sn:[13, 14, 48]
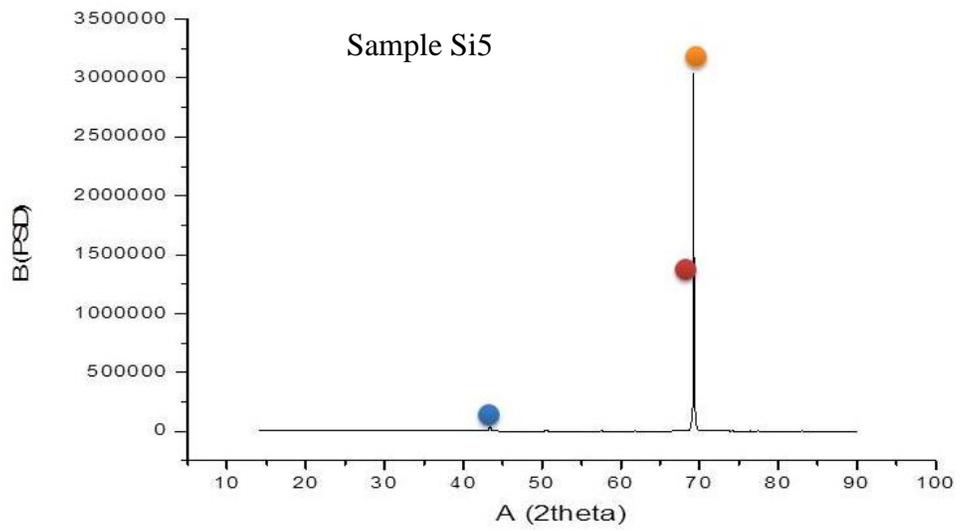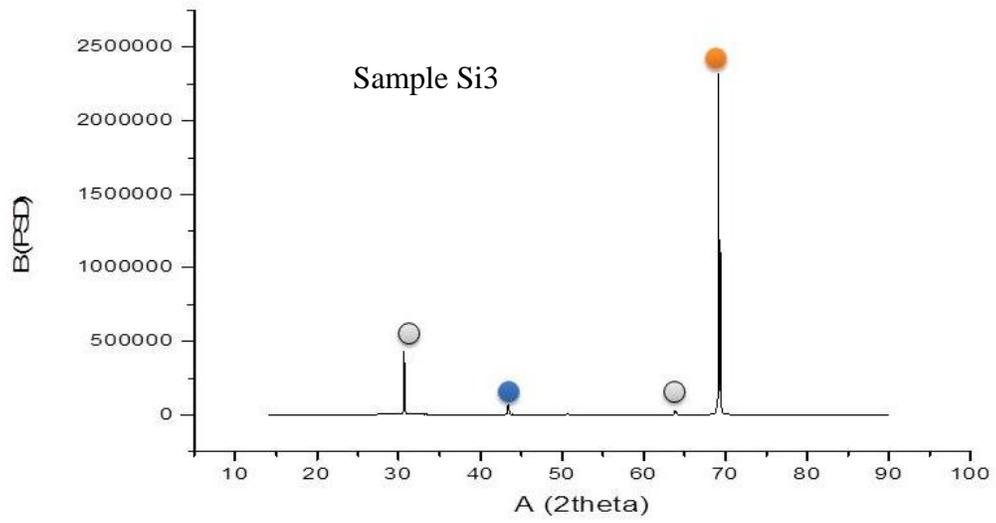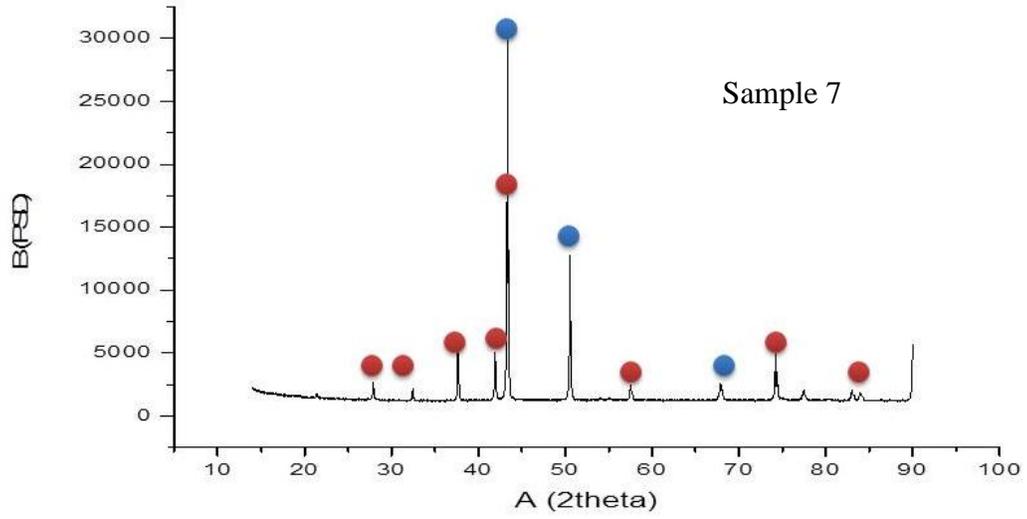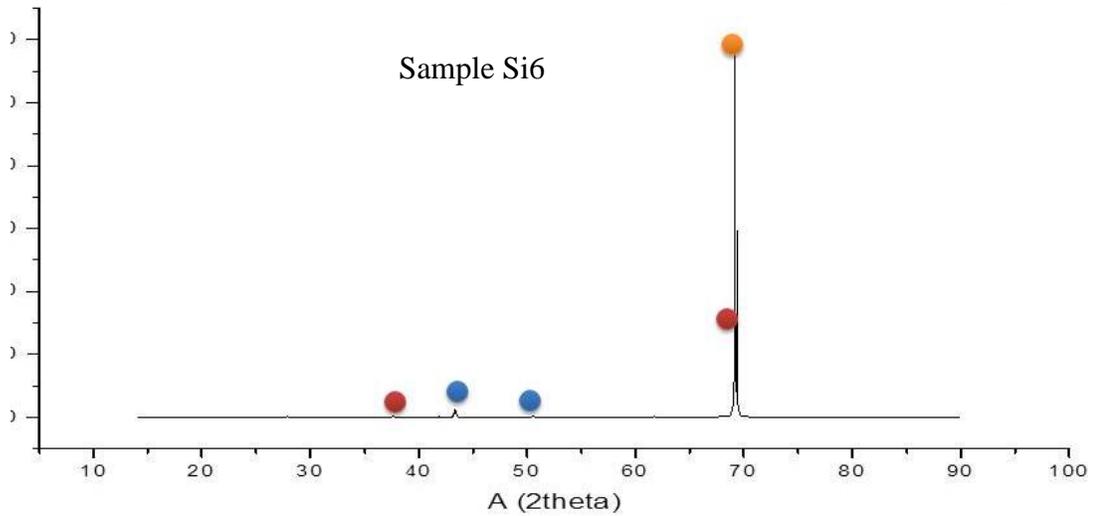

CuSn:[13, 14]

36
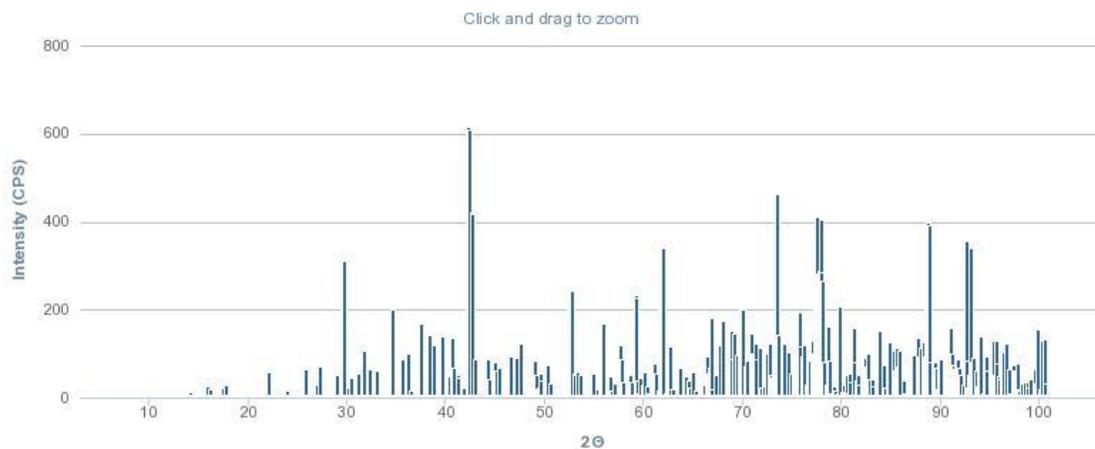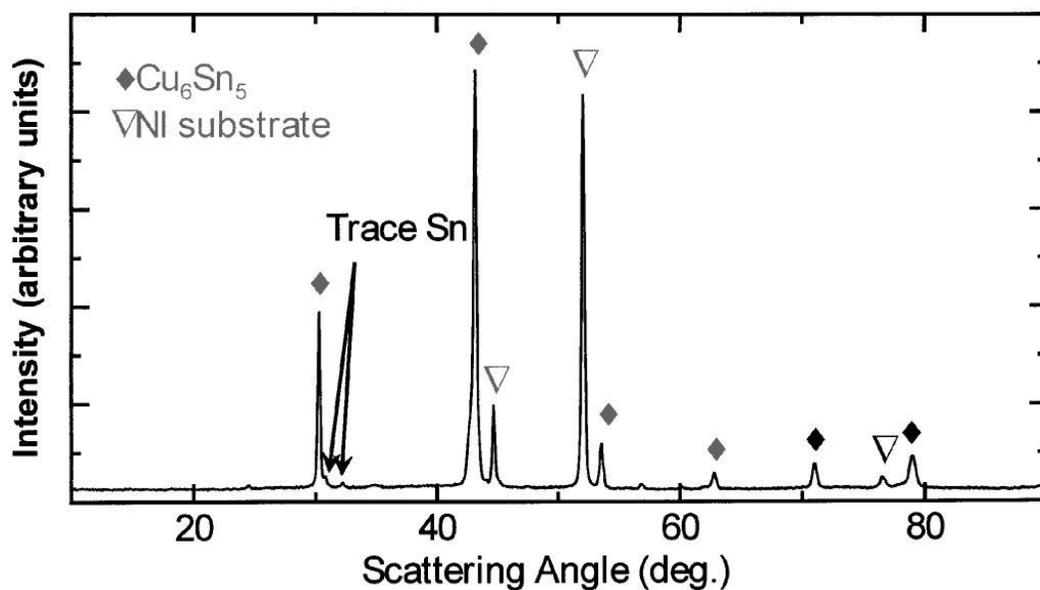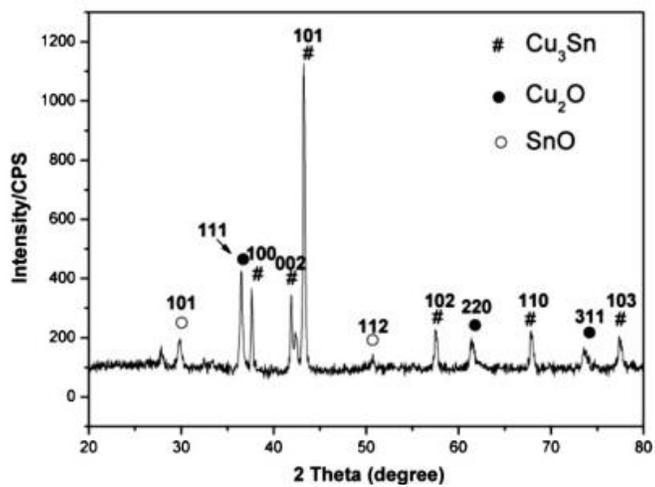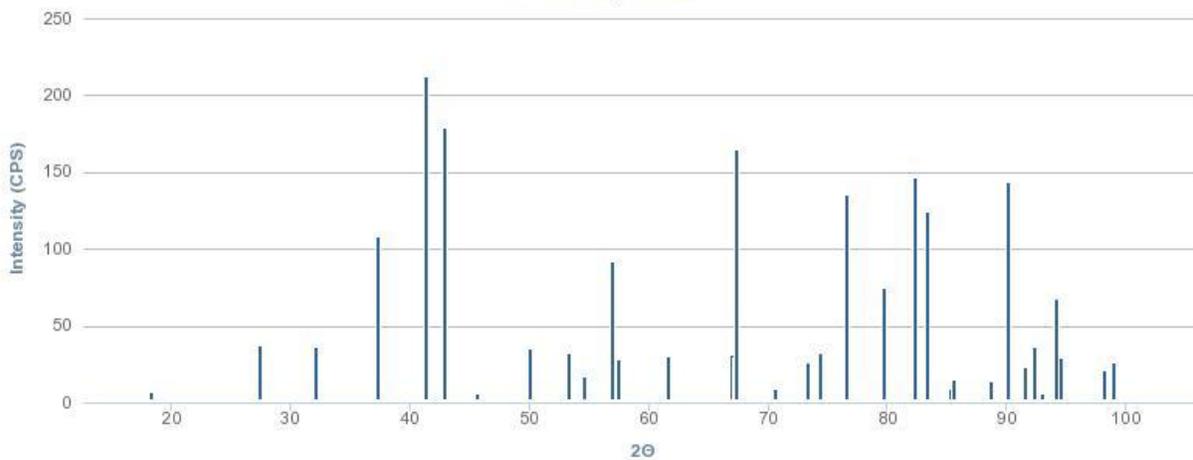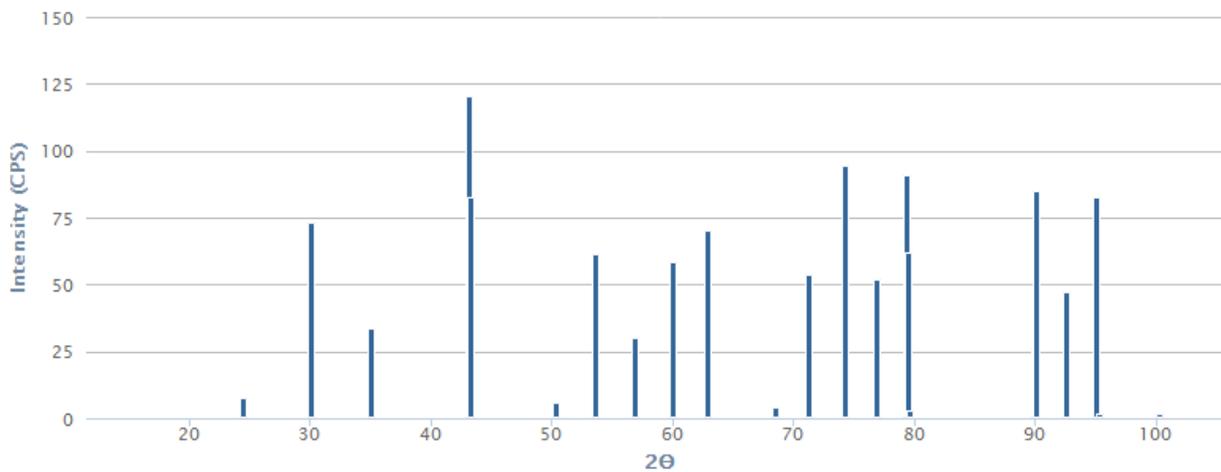
Sample Diffractograms:

Key: Blue = Cu; Grey = Sn; Red = Cu_3Sn; Black = Cu_6Sn_5; Orange = Si.

Sample 1

Sample 3

Sample 5

Sample 6

Sample 1a

Sample 3a

Sample 5a

Sample 6a

Sample 7

Sample Si3

Sample Si5

Sample Si6

A (2theta)
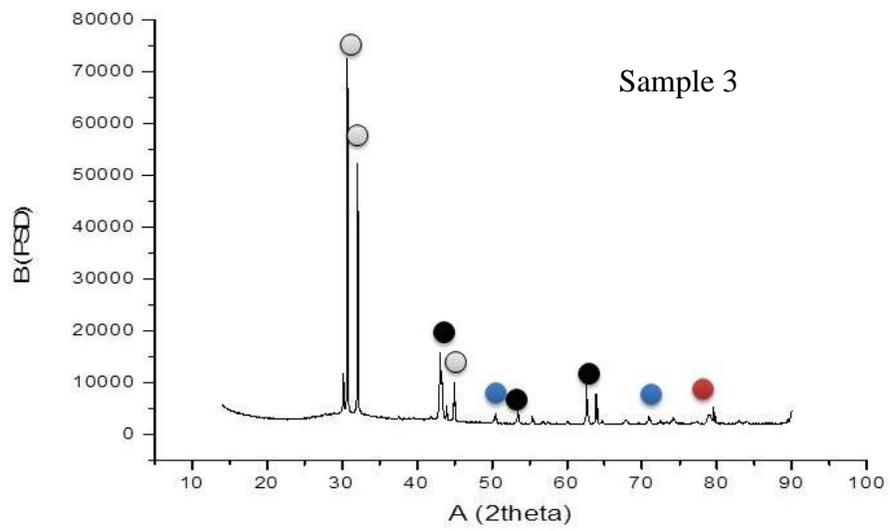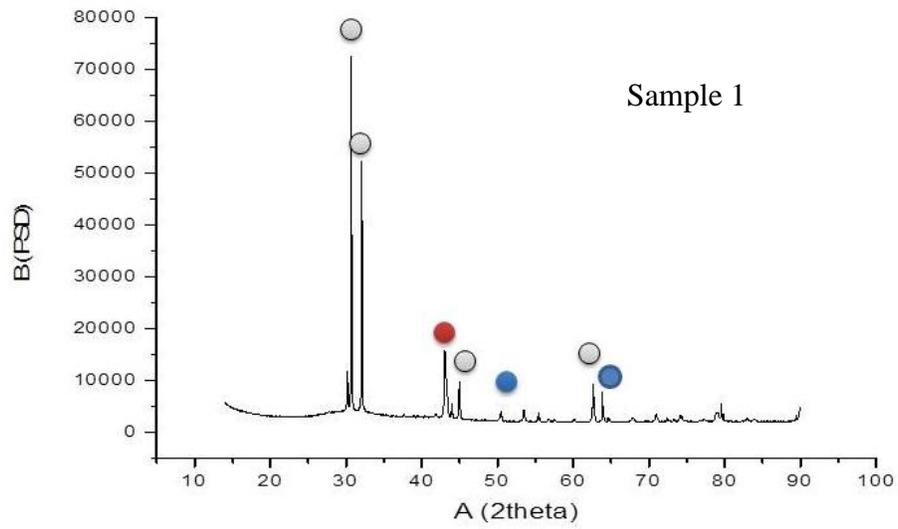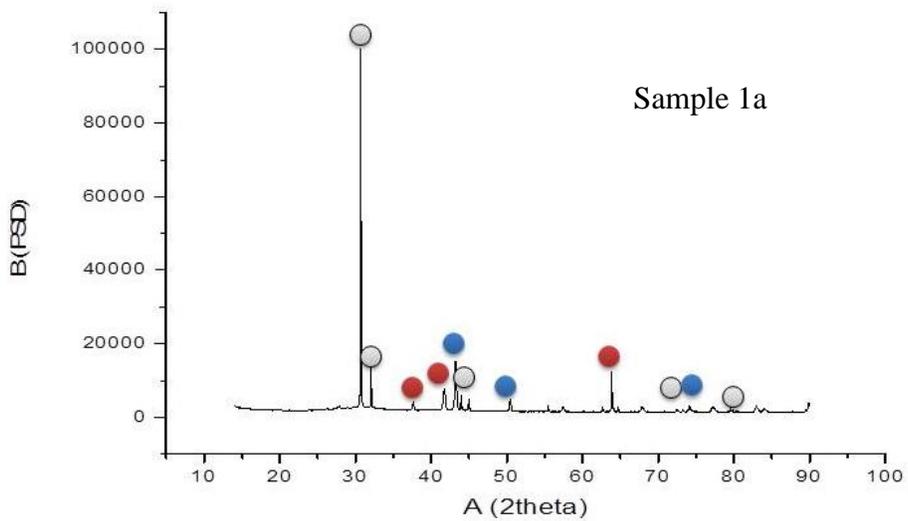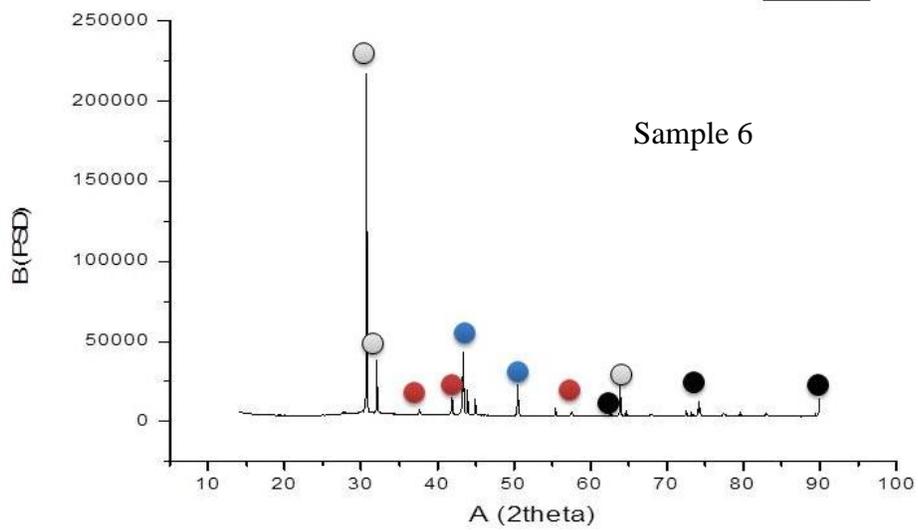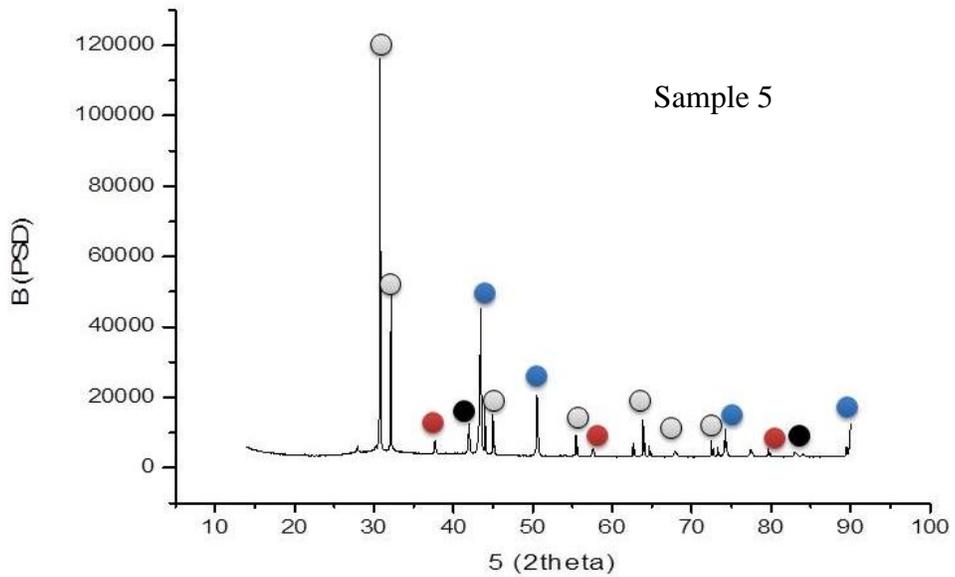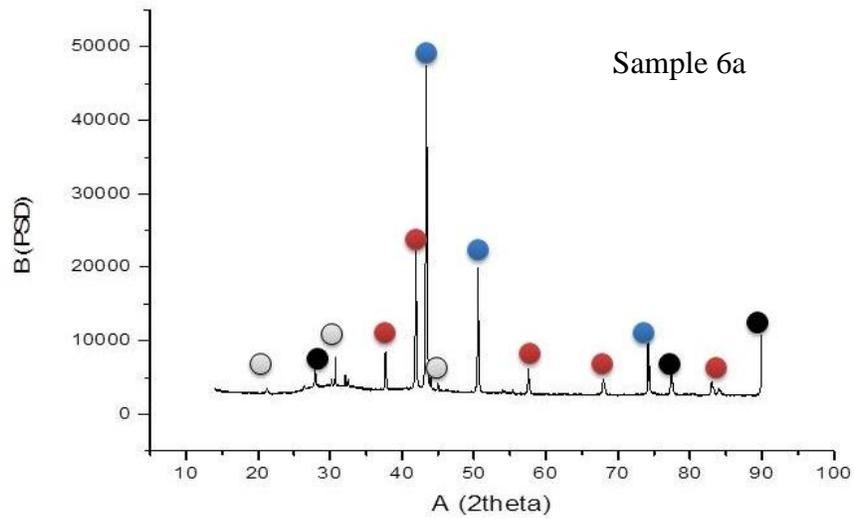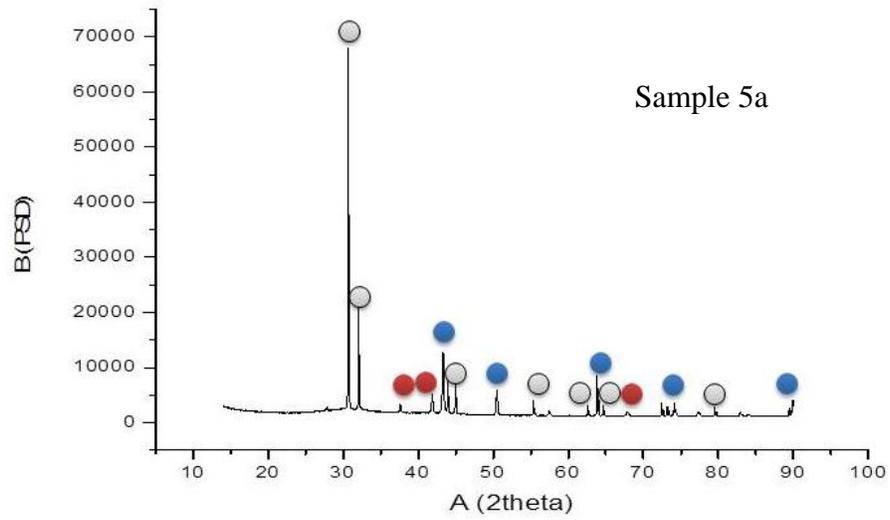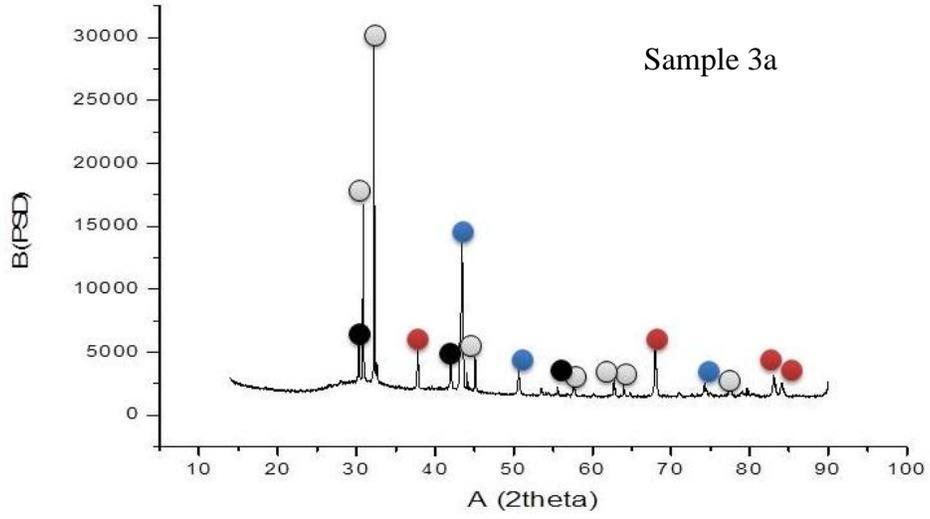
Appendix B: Electrochemical Impedance Spectroscopy:

Sample 7

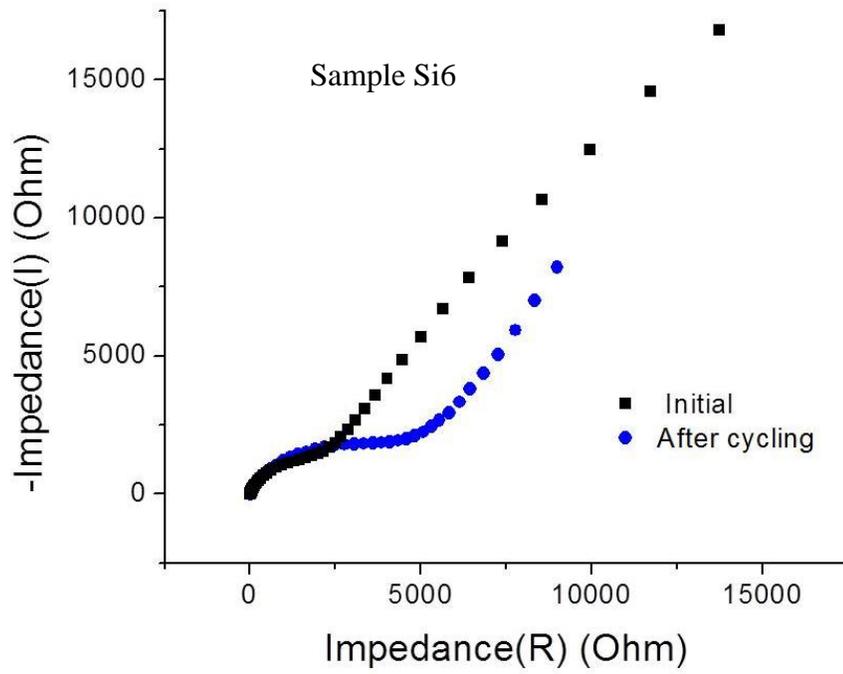■ Initial
● After cycling
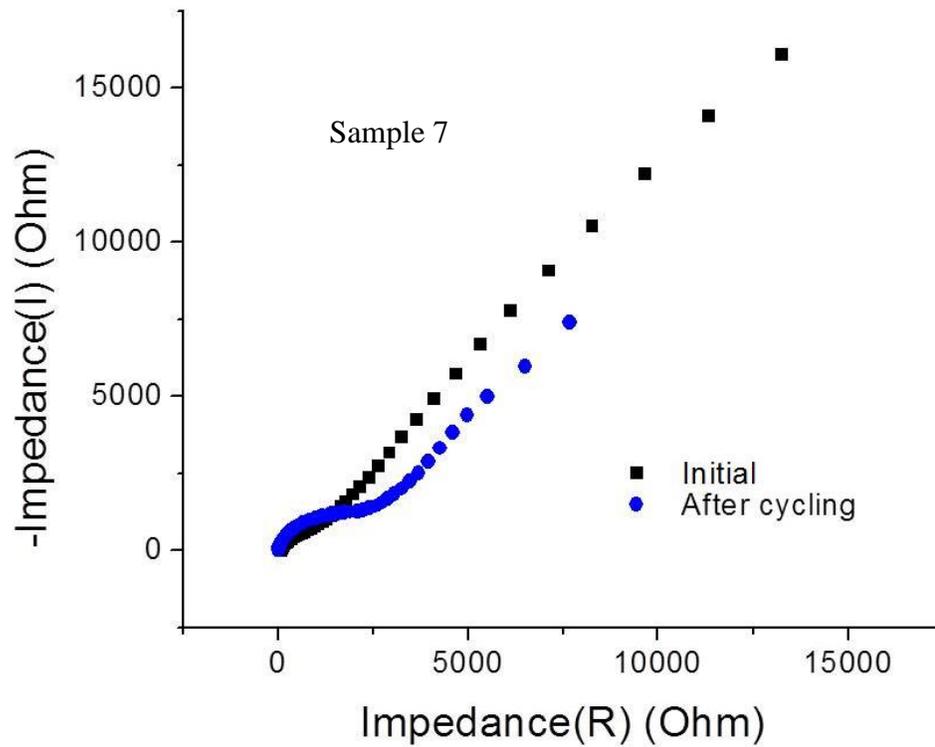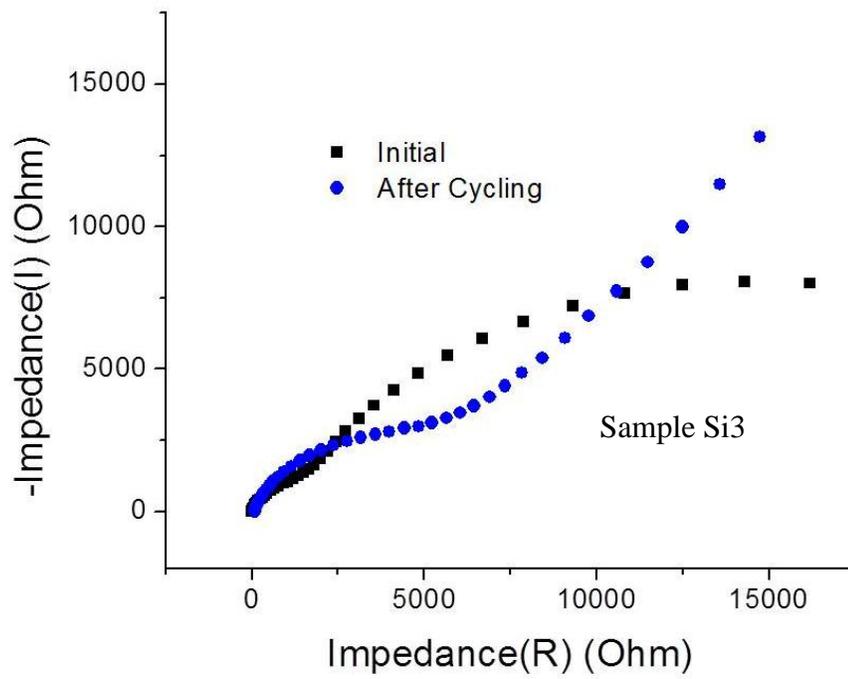
References:

1.	Hoffert, M. I.; Caldeira, K.; Benford, G.; Criswell, D. R.; Green, C.; Herzog, H.; Jain, A. K.; Kheshgi, H. S.; Lackner, K. S.; Lewis, J. S.; Lightfoot, H. D.; Manheimer, W.; Mankins, J. C.; Mauel, M. E.; Perkins, L. J.; Schlesinger, M. E.; Volk, T.; Wigley, T. M. L., Advanced Technology Paths to Global Climate Stability: Energy for a Greenhouse Planet. *Science* 2002, 298, 981-987.

2.	Chevrier, V. L.; Ceder, G., Challenges for Na-ion Negative Electrodes. *Journal of The Electrochemical Society* 2011, 158, A1011-A1014.

3.	Wadia, C.; Albertus, P.; Srinivasan, V., Resource constraints on the battery energy storage potential for grid and transportation applications. *Journal of Power Sources* 2011, 196, 1593-1598.

4.	Kim, S.-W.; Seo, D.-H.; Ma, X.; Ceder, G.; Kang, K., Electrode Materials for Rechargeable Sodium-Ion Batteries: Potential Alternatives to Current Lithium-Ion Batteries. *Advanced Energy Materials* 2012, 2, 710-721.

5.	Slater, M. D.; Kim, D.; Lee, E.; Johnson, C. S., Sodium-Ion Batteries. *Advanced Functional Materials* 2012, n/a-n/a.

6.	Kepler, K. D.; Vaughey, J. T.; Thackeray, M. M., LixCu6Sn5 (0<x<13) : An Intermetallic Insertion Electrode for Rechargeable Lithium Batteries. *Electrochemical and Solid-State Letters* 1999, 2, 307-309.

7.	Beattie, S. D.; Dahn, J. R., Single Bath, Pulsed Electrodeposition of Copper-Tin Alloy Negative Electrodes for Lithium-ion Batteries. *Journal of The Electrochemical Society* 2003, 150, A894-A898.

8.	Massalski, T. B.; Murray, J. L.; Bennett, L. H.; Baker, H., *Binary alloy phase diagrams*. American Society for Metals: Metals Park, Ohio, 1986.

9.	Baggetto, L.; Jumas, J.-C.; Gorka, J.; Bridges, C. A.; Veith, G., Predictions of particle size and lattice diffusion pathway requirements for sodium-ion anodes using eta-Cu6Sn5 thin films as a model system. Oak Ridge National Laboratories: 2013; pp 1-43.

10.	Stegmaier, S.; Fassler, T. F., A Bronze Matryoshka: The Discrete Intermetalloid Cluster Sn@Cu-12@Sn-20 (12-) in the Ternary Phases A(12)Cu(12)Sn(21) (A = Na, K). *Journal of the American Chemical Society* 2011, 133, 19758-19768.

11.	Stegmaier, S.; Fassler, T. F., Na2.8Cu5Sn5.6: A Crystalline Alloy Featuring Intermetalloid (1)(infinity){Sn-0.6@Cu-5@Sn-5} Double-Walled Nanorods with Pseudo-Five-Fold Symmetry. *Angewandte Chemie-International Edition* 2012, 51, 2647-2650.

12.	Meng, Y. S.; Arroyo-de Dompablo, M. E., First principles computational materials design for energy storage materials in lithium ion batteries. *Energy & Environmental Science* 2009, 2, 589-609.

13.	Ong, S. P.; Jain, A.; Hautier, G.; Kocher, M.; Cholia, S.; Gunter, D.; Bailey, D.; Skinner, D.; Persson, K.; Ceder, G., The Materials Project.

14.	Jain, A.; Hautier, G.; Moore, C. J.; Ong, S. P.; Fischer, C. C.; Mueller, T.; Persson, K. A.; Ceder, G., A high-throughput infrastructure for density functional theory calculations. *Computational Materials Science* 2011, 50, 2295-2310.

15.	Ong, S. P.; Richards, W. D.; Jain, A.; Hautier, G.; Kocher, M.; Cholia, S.; Gunter, D.; Chevrier, V. L.; Persson, K. A.; Ceder, G., Python Materials Genomics (pymatgen): A robust, open-source python library for materials analysis. *Computational Materials Science* 2013, 68, 314-319.

16.	Kresse, G.; Marsman, M.; Furthmuller, J. Vienna Ab-initio Software Package 2012.

17.   Courtney, I. A.; Tse, J. S.; Mao, O.; Hafner, J.; Dahn, J. R., Ab initio calculation of the lithium-tin voltage profile. *Physical Review B* 1998, 58, 15583-15588.

18.   Mo, Y., 2013.

19.   Zhu, X.; Chen, N.; Lian, F.; Song, Y.; Li, Y., First principle calculation of lithiation/delithiation voltage in Li-ion battery materials. *Chinese Science Bulletin* 2011, 56, 3229-3232.

20.   Aydinol, M. K.; Kohan, A. F.; Ceder, G.; Cho, K.; Joannopoulos, J., Ab initio study of lithium intercalation in metal oxides and metal dichalcogenides. *Physical Review B* 1997, 56, 1354-1365.

21.   Onishi, M.; Fujibuchi, H., Reaction-Diffusion in the Cu-Sn System. *Transactions of the Japanese Institute of Metals* 1975, 16, 539 - 547.

22.   Kumar, S.; Handwerker, C. A.; Dayananda, M. A., Intrinsic and Interdiffusion in Cu-Sn System. *Journal of Phase Equilibria and Diffusion* 2011, 32, 309-319.

23.   Paul, A.; Ghosh, C.; Boettinger, W. J., Diffusion Parameters and Growth Mechanism of Phases in the Cu-Sn System. *Metallurgical and Materials Transactions a-Physical Metallurgy and Materials Science* 2011, 42A, 952-963.

24.   Mei, Z.; Sunwoo, A. J.; Morris, J. W., ANALYSIS OF LOW-TEMPERATURE INTERMETALLIC GROWTH IN COPPER-TIN DIFFUSION COUPLES. *Metallurgical Transactions a-Physical Metallurgy and Materials Science* 1992, 23, 857-864.

25.   Chromik, R. R.; Cotts, E. J., Thermodynamic and Kinetic Study of Phase Transformations in Solder/Metal Systems. *MRS Online Proceedings Library* 1996, 445, null-null.

26.   Chao, B.; Chae, S. H.; Zhang, X. F.; Lu, K. H.; Im, J.; Ho, P. S., Investigation of diffusion and electromigration parameters for Cu-Sn intermetallic compounds in Pb-free solders using simulated annealing. *Acta Materialia* 2007, 55, 2805-2814.

27.   Vianco, P. T.; Erickson, K. L.; Hopkins, P. L., SOLID-STATE INTERMETALLIC COMPOUND GROWTH BETWEEN COPPER AND HIGH-TEMPERATURE, TIN-RICH SOLDERS .1. EXPERIMENTAL-ANALYSIS. *Journal of Electronic Materials* 1994, 23, 721-727.

28.   Kidson, G. V., SOME ASPECTS OF THE GROWTH OF DIFFUSION LAYERS IN BINARY SYSTEMS. *Journal of Nuclear Materials* 1961, 3, 21-29.

29.   Campbell, S. A., *Fabrication Engineering at the Micro- and Nanoscale*. 3 ed.; Oxford University Press: New York, 2008 p648.

30.   Jones, D. A., *Principles and prevention of corrosion*. Prentice Hall: Upper Saddle River, NJ, 1996.

31.   Low, C. T. J.; Walsh, F. C., The stability of an acidic tin methanesulfonate electrolyte in the presence of a hydroquinone antioxidant. *Electrochimica Acta* 2008, 53, 5280-5286.

32.   Gernon, M. D.; Wu, M.; Buszta, T.; Janney, P., Environmental benefits of methanesulfonic acid: Comparative properties and advantages. *Green Chemistry* 1999, 1, 127-140.

33.   Wan, J.; Chen, Y., 2013.

34.   Bader, S.; Gust, W.; Hieber, H., RAPID FORMATION OF INTERMETALLIC COMPOUNDS BY INTERDIFFUSION IN THE CU-SN AND NI-SN SYSTEMS. *Acta Metallurgica Et Materialia* 1995, 43, 329-337.

35.   Egerton, R. F. Physical principles of electron microscopy an introduction to TEM, SEM, and AEM. http://public.eblib.com/EBLPublic/PublicView.do?ptiID=264884.

36.   Bard, A. J.; Faulkner, L. R., *Electrochemical methods : fundamentals and applications*. Wiley: New York, 1980.

37.   *EC-Lab Software Techniques and Applications*. 10.1x ed.; France, 2011.

38.   Huggins, R. A. Advanced batteries materials science aspects. http://site.ebrary.com/id/10266256.

39.   Wedepohl, K. H., THE COMPOSITION OF THE CONTINENTAL-CRUST. *Geochimica Et Cosmochimica Acta* 1995, 59, 1217-1232.

40.   Morales, J., Zager, M., Ed. 2013.

41.   Low, C. T. J.; Walsh, F. C., Electrodeposition of tin, copper and tin-copper alloys from a methanesulfonic acid electrolyte containing a perfluorinated cationic surfactant. *Surface & Coatings Technology* 2008, 202, 1339-1349.

42.   Verma, P.; Maire, P.; Novák, P., A review of the features and analyses of the solid electrolyte interphase in Li-ion batteries. *Electrochimica Acta* 55, 6332-6341.

43.   Balbuena, P. B.; Wang, Y., *Lithium-ion batteries : solid-electrolyte interphase*. Imperial College Press: London, 2007.

44.   Datta, M. K.; Epur, R.; Saha, P.; Kadakia, K.; Park, S. K.; Kumta, P. N., Tin and graphite based nanocomposites: Potential anode for sodium ion batteries. *Journal of Power Sources* 2013, 225, 316-322.

45.   Komaba, S.; Murata, W.; Ishikawa, T.; Yabuuchi, N.; Ozeki, T.; Nakayama, T.; Ogata, A.; Gotoh, K.; Fujiwara, K., Electrochemical Na Insertion and Solid Electrolyte Interphase for Hard-Carbon Electrodes and Application to Na-Ion Batteries. *Advanced Functional Materials* 2011, 21, 3859-3867.

46.   Henkelman, G.; Jonsson, H., Improved tangent estimate in the nudged elastic band method for finding minimum energy paths and saddle points. *Journal of Chemical Physics* 2000, 113, 9978-9985.

47.   Ma, W. Y.; Zhou, B.; Wang, J. F.; Zhang, X. D.; Jiang, Z. Y., Effect of oxygen vacancy on Li-ion diffusion in a V2O5 cathode: a first-principles study. *Journal of Physics D-Applied Physics* 2013, 46, 8.

48.   Li, Z. W.; Li, X. H.; Tao, X. J.; Zhang, Z. J.; Yu, L. G., Preparation and characterization of Cu3Sn nanoparticles via a facile ultrasonic irradiation. *Materials Letters* 2012, 67, 142-144.